Soft tissue histology of insect larvae decayed in laboratory experiments using microbial mats: Taphonomic comparison with Cretaceous fossil insects from the exceptionally preserved biota of Araripe, Brazil

Miguel Iniesto, Paula Gutiérrez-Silva, Jaime Dias, Ismar Carvalho, Angela Buscalioni, Ana Isabel López-Archilla

Soft tissue histology of insect larvae decayed in laboratory experiments using microbial mats: taphonomic comparison with Cretaceous fossil insects from the exceptionally preserved biota of Araripe, Brazil

Iniesto, Miguel [a,b,]; Gutiérrez-Silva, Paula [a]; Dias, Jaime J.[c]; Carvalho, Ismar S.[c]; Buscalioni, D. Ángela [d] ; López-Archilla, Ana Isabel [a]

[a] *Department of Ecology, Universidad Autónoma de Madrid, 28049 Madrid, Spain, anabel.lopez@uam.es;*

[b] *Diversity, Ecology and Evolution of Microbes Laboratory, Unité d'Ecologie Systématique et Evolution UMR 8079, CNRS, Université Paris-Saclay, AgroParisTech, 91405 Orsay, France, miguel.iniesto@u-psud.fr;*

[c] *Department of Geology, Universidade Federal do Rio de Janeiro, 21.949-900 Rio de Janeiro, Brazil; jaimejoaquimdias@gmail.com, ismar@geologia.ufrj.br;*

[d] *Department of Biology, Universidad Autónoma de Madrid, 28049 Madrid, Spain, and CIPb (Centre for the integration of Paleobiology), angela.delgado@uam.es.*

Corresponding author:

Miguel Iniesto. miguel.iniesto@gmail.com

Present address: Équipe DEEM, Laboratoire ESE, Université Paris-Saclay, 362 Rue du Doyen André Guinier, 91405 Orsay, France

Abstract

Experimental taphonomy using microbial mats offers new insights into the mechanisms involved in the decay of organisms and their preservation as fossils. In this paper, the experimental decay products of soft-bodied insect larvae (the greater wax moth, *Galleria mellonella*, and the mealworm, *Tenebrio molitor*) in microbial mats have been described and compared with those of grylloid fossils derived from the Cretaceous Crato Formation of Brazil. This novel approach characterises the decay and mineralisation of different tissues (cuticle, gut tract, silk gland, trachea, and fat body tissues) using transverse histological sections. Multivariate seriation statistics using histology indicate a significant non-random process, in which the two species show the same general decay sequence, namely: decay of fat bodies and muscles on Day 11, digestive degradation and occurrence of endogenous bacteria on approximately Day 30, and degradation of cuticles and tracheal networks (the most perdurable) on Days 60 and 120, respectively. Principal component analysis, based on the qualitative features of the decaying state of tissues, showed that the greatest alterations occurred between Days 60 and 180 in the controls without mats; however, in the microbial mat experiments, larvae showed better preservation overall. Based on scanning electron microscopy and energy-dispersive X-ray spectroscopy, mineralisation of the larvae extends outside the cuticle and inner tissues. The predominance of certain anions (sulfate, chloride, and phosphate) is associated with the microbial activity of the mat community and the composition of water. The organic mesh of exopolymeric substances and cyanobacteria enriched in elements (e.g., Na and Mg) formed an amorphous crust that covered the larval body. This crust is similar to the massive crystallised external film found on the grylloid fossils derived from the Crato Formation of Brazil. The minerals were found to vary with

location and time, with sulfates appearing mostly internally and for longer periods. Sulfurisation is discussed as the principal preservation process and is rapid in the early stages of organic matter decay. This comparison between the outcomes produced by taphonomic experiments using actual microbial mats and exceptionally preserved fossils can provide valuable information to understand more about the formation of numerous Konservat-Lagerstätten.

Keywords: experimental taphonomy, insects, decay, fossilisation, sulfurization, Crato Formation.

1. Introduction

Experimental taphonomy is becoming an important scientific discipline, defining its own terminology, targeting the major processes involved in fossilisation (decay, mineralisation, and maturation), and providing data on controlled experimental variables (see Samson, 2014 for a detailed review). The goal of experimental taphonomy is to explore some of the critical processes that favour soft-tissue preservation under controlled short-term laboratory conditions by simplifying and isolating the factors and variables involved in those processes (Briggs and McMahon, 2016; Purnell et al., 2018). Significant studies have provided information on, for instance, phylogenetic signals and taphonomic decay (Sansom et al., 2010; Button et al., 2012; Murdock et al., 2016), optimum environmental conditions and mineralisation types (Briggs and Wilby, 1996; Channing and Edwards, 2004; Slater et al., 2020), and an understanding of the maturation process by replicating factors such as temperature and pressure (Bernard et al., 2007; Gäb et al., 2020).

Experimental taphonomy is a reductionist approach, and no direct and simple causal link exists between decay and preservation (e.g., Purnell et al., 2018). However, the experimental

designs and analytical approaches in this field are necessary to understand the interconnections between decay and mineralization and, thereby, to detect potential taphonomic challenges such as differential preservation in fossils (e.g. Briggs and Kear, 1993; Sagemann et al., 1999; Iniesto et al., 2013, 2016; Klompmaker et al., 2017; Purnell et al., 2018). Taphonomic experimentation cannot yet replicate in a laboratory the physiochemical conditions that occurred in every ancient environment and putatively influenced the genesis of exceptional deposits. Nonetheless, every publication in this field is a step towards understanding key processes in exceptional preservation, with the greatest focus on estimating the time intervals of the early decay and burial phases (e.g., Iniesto et al., 2013; Alleon et al., 2016), the sequences of observed decay and tissue preservation (e.g., Briggs and Kear 1993; Sagemann et al., 1999; Sansom et al., 2010, 2011, Iniesto et al. 2013), and/or the physical and chemical conditions that enhance fossilisation and biomolecular preservation (e.g., Jacquemot et al., 2019; Gutpta 2010; Li et al., 2014) .

Considering the need for a greater number of more precise actuotaphonomical studies, one of the pending issues is to obtain data from experimentation using microbial mats (Briggs and McMahon, 2016). Unlike biofilms, which have low diversity and are frequently dominated by a small number of populations, mats are formed by an extremely complex microbial community that is dominated, in most cases, by autotrophic microorganisms (Stal, 2012). Therefore, experiments with microbial mats offer the best chance of tracking the ecology of the decay processes, characterising the biotic and abiotic factors, and exploring the interactions between microbial mats and organic remains.

To fill knowledge gaps, we produced assays with distinct selected organisms (fish, frogs, flies, and ferns), and placed the carcasses and organic remains on mats grown under controlled conditions (Iniesto et al., 2013, 2015a, 2015b, 2017, 2018). Microbial mats introduce novel questions to taphonomic experiments, because mats are dominated by

autotrophs and oxygen-generating microorganisms, which are able to maintain an oxygenated environment inside and outside the carcass and a high pH for a longer period of time (Iniesto et al., 2015a). The presence of mats has been linked to the formation of dead masks (Gehling, 1999; Darroch et al., 2012), the generation of detailed replicas and negative imprints (Iniesto et al., 2016), and mineralisation that can be produced even under alkaline and oxic conditions (Iniesto et al., 2015b). Additionally, the presence of microbes is considered relevant in the preservation and fossilisation of several Konservat Lagerstätten that appear in the continental Mesozoic localities, such as of Las Hoyas (Delclòs et al., 2004; Delclòs and Soriano, 2016) and Araripe (Menon and Martill, 2007), and in the Miocene of Rubielos de Mora (Peñalver-Mollá, 2002) and Libros (McNamara et al., 2016),

The present study explores the decay and mineralisation of larvae from two insect taxa (Lepidoptera and Coleoptera). We characterised biostratinomic and early diagenetic alterations and compared the decay chronology with studies of other soft-bodied organisms. We described changes in the external and internal morphology and composition of the larvae, according to their qualitative features, and analysed the ongoing processes of mineralisation using elemental mapping of various body parts. The sequence of decay and mineralisation of tissues (i.e., gut tract, cuticle, fat body, trachea, and silk gland tissues) was also monitored. We combined a variety of techniques to contrast the results obtained via histological sections, tissues, and bacterial staining using magnetic resonance imaging (MRI) and/or scanning electron microscopy coupled with energy-dispersive X-ray spectroscopy (SEM-EDXS). Finally, we compare these experimental results with the taphonomic analyses performed on fossil insects from the Early Cretaceous Crato Formation (Araripe Basin Brazil) (Osés et al., 2016, 2017; Dias and Carvalho, 2020).

2. Materials and methods

The experimental protocol followed that of Iniesto et al. (2013), using microbial mats grown under laboratory conditions with control cultivation chambers as a reference. Samples of the mats, water, and sediment were collected at the Salada de Chiprana shallow lake in the semiarid region of the Ebro depression (Zaragoza province, Spain) (Fig. 1A). The lake water is characterized by a high concentration of magnesium and sulfate ions (Supplementary Table S1) in addition to other ions (e.g., sodium, calcium, and phosphate) in smaller quantities (Jonkers et al., 2003). The composition of Salada de Chiprana's sediments includes major mineral phases of quartz and gypsum, although they also contain kieserite (an evaporitic hydrated magnesium sulfate), aragonite, and some other carbonated minerals (Iniesto et al., 2015b).

2.1 Mat growth

To assure a homogeneous distribution of the different microbial populations, mat samples were crushed and grown in glass chambers (Iniesto et al., 2013, 2016). For this experiment, the microbial mats were grown for 6 months (until mats acquired their characteristic layered organization and presented pinnacles in the surface) in three 42 cm × 18 cm × 20 cm cultivation chambers exposed simultaneously to both ambient and LED lighting while maintaining day/night periods of 12 hours. The fourth cultivation chamber was inoculated but kept in complete darkness and used as the control. The abiotic variables related to mat growth are shown in Supplementary Table S1.

The Chiprana microbial mat surface presents a typical honeycomb pattern with ridges and tufts (Fig. 1B), possibly containing some microbially induced sedimentary structures (MISS) (Noffke et al., 2001; Noffke and Awramik, 2013). This cultivated mat, as well as the natural microbial mat collected in Chiprana, are dominated by photosynthetic microorganisms, especially cyanobacteria *Coleofasciculus* (*Microcoleus*) *chthonoplastes* that

coexist with anoxygenic phototrophic bacterium of the green nonsulfur family of Chloroflexaceae (Fourçans et al., 2004; De Wit, 2016). The thickness of this green top layer of the mat ranges from 0.7 to 1.2 mm. In addition, located beneath the top layers, other anoxygenic phototrophs appear, including green and red sulfur bacteria and a plethora of chemoorganoheterotrophs and chemilithotrophs of both aerobic and anaerobic populations (Fig. 1C). Therefore, the environmental factors, such as light penetration, dissolved oxygen (DO), pH, and redox potential, to which the whole community is subjected, vary greatly in depth. The DO varies from 430 µM at the surface of the mat to a maximum of 449 µM just below and decreases to practically 0 µM at the limit between the mat and underlying sediment. The pH is markedly basic (10.2) just above the mat´s photosynthetic layer and decreases to 8.7 in the sediment (data reported in Iniesto et al., 2015a).

2.2 The model organisms

Two different holometabolous insect species, *Galleria mellonella* (Order Lepidoptera, Pyealidae) and *Tenebrio molitor* (Order Coleoptera, Tenebrionidae), were selected because their larvae are well-known anatomically, easily allow manipulation, and have simple outer and inner anatomy that facilitate taphonomic observations. Both species are commonly used in experimental designs. *G. mellonella* is often used as a model for taphonomic experiments (Darroch et al., 2012) and immunological research because its immune responses share similarities to those of vertebrates (Pereira et al., 2015). *T. molitor* constitutes an economical resource for pet food because of its high protein and fat content (Park et al., 2014). These two species are ecologically important because they are able to degrade wax and long chains of hydrocarbons with the help of intestinal microbiota (Kong et al., 2019).

These two larvae have three thoracic segments with six legs terminally ending in a sclerotized hook. The larva of *G. mellonella* (popularly known as the wax moth) is about 25

mm in size at the last instar prior to pupation and bears four pairs of prolegs at the third to sixth abdominal segments (Fig. 2A). Most of the larva is soft, but some areas (the head, thoracic leg, and anal region) are sclerotized (Smith, 1965). The *T. molitor* larva is commonly referred to as a mealworm (Fig. 2B) and measures about 25 mm; its stadia length (between the 3–9 instars) is also extremely regular (Morales-Ramos et al., 2010). The mealworm has a thicker exocuticle than the wax moth; this thickness is linked to epidermal melanization (Hajek and St. Leger, 1994).

The epidermis, gut tract, tracheal network, fat bodies, and silk gland were selected to trace the inner taphonomic alterations of these larvae. These tissues differ in their epithelial features for every histological organization (Figs. 2 and 3 E-H) and represent a variety of systems (integument, digestive, respiratory and excretory, and muscular) and organs (silk gland). The integument includes three layers with an exocuticle composed of lipids and proteins (Neville, 1975; Roberts and Willis, 1980). The epidermis is separated from the underlying tissues by a thin matrix called the basal lamina (Vigneron et al., 2019). The digestive tract consists of three regions, the foregut (stomatodaeum), the midgut (mesenteron), and the hindgut (proctodaeum). The midgut is the primary site of digestion and absorption and lacks the exoskeletal chitin lining seen in the foregut and hindgut (Neville, 1975; Borror et al., 1989). The midgut has the basic tissue architecture characteristic of epithelial columnar cells. It possesses a peritrophic matrix of mucus surrounding the digestive tract (Emery et al., 2019). The *T. molitor* digestive tract is dominated by Malpighi tubules (Figs. 2B and 3F) that correspond to a well-developed excretory system. The Malpighian tubule system is formed by a single cell-layered epithelial tube (King and Denholm, 2014). The respiratory system comprises a network of gas-filled, cuticle-lined tubes of trachea and tracheoles, which form paired and branch series along the body segments (Raś et al., 2018). The somatic muscular system, composed of myoglobin fibers, is arranged in ventral and dorsal bunches in short

single medial, lateral, and oblique muscles that are packed with nerves, connective tissue, and ganglions. The fat body tissue comprises cells (trophocytes, a type of adipocyte that stores energy) in close contact with the insect hemolymph. The trophocytes are held together to form sheets of tissues clothed in a basal lamina (Hoshizaki, 2013). Finally, the wax moth produces silk through its salivary glands. The silk gland begins dorsally in the fifth abdominal segment and moves forward, widening into a mid-silk gland (MSG, Fig. 2A) with three or more loops. The MSG is located ventrally in the digestive tract and narrows into a much thinner anterior part towards the mouth. The MSG has a large lumen that acts as a reservoir for silk proteins (fibroin and serine) that are secreted by the posterior silk gland (PSG) (Andersson et al., 2016; Kludkiewicz et al., 2019).

2.3 Experimental design, data, and techniques

The specimens were euthanized following the Research Ethics Committee (CEI-UAM) protocol with 0.1 gr of tricaine methanesulfonate (MS222; SIGMA-ALDRICH E10521-10G) and 0.87 gr of TRIS phosphate buffer dissolved in 300 ml of distilled water. The specimens were submerged for 5 minutes, followed by four washes with physiological serum to remove the lethal solution. A total of twenty-four larvae were placed in each cultivation chamber (96 carcasses in total, twelve specimens of each species in three cultivation chambers on microbial mats, and one on the sediment) (Fig. 3 A-B). Then, five individuals per species were randomly chosen at day 4, 11, 30, 60, 120, and 180. Each time, two individuals (from the control and from the mat) underwent preparation for histological section staining with eosin and hematoxylin, while two others were directly analyzed by MRI. The remaining fifth specimen was used for SEM and EDXS. The specimens for histological analysis and SEM-EDX were fixed with 2.5% glutaraldehyde (in 0.1 M cacodylate buffer) in a vacuum for 48 hours. A cacodylate buffer was used to stabilize the pH. Subsequently, the

samples were dehydrated by successive immersion in 30%, 50%, 70%, and 100% ethanol solutions (one hour in each bath). Samples were kept in 100% ethanol until observation.

MRI subjects specimens to a high magnetic field and pulsed radio waves that allow the mapping of hydrogen atoms within samples (especially those contained in water) and is thus utilized for the observation of soft tissues (Pebet, 2004) (Fig. 4 and Fig S1). In T2-weighted images, more hydrated organs have higher signals (Novelline, 2004). MRI was performed at the Pluridisciplinary Institute of UCM using a Bruker BMT 47/40 MRI scanner (Grimm et al., 2003; Riches et al., 2009). Images from 10 samples (taken at days 0, 30, and 180) were subsequently analyzed using Fiji (Schindelin et al., 2012). This analyzer visualizes a specimen in 2D sections that can be stacked in a 3D model using the MRI File Manager (Bruker) plugin (Montigon, 2006) for Fiji. .

For the histological sections, the specimens were included in paraffin after fixation and dehydration, and sectioned into 4 μm thick slices at the Department of Histology at the National Center for Biotechnology (CNB, UAM). The anterior and the posterior parts of the larvae were longitudinally sectioned, whereas the areas between the first and sixth abdominal segments were transversely sectioned (Figs. 5 and 6). The sections were dewaxed in xylene (10 minutes × 2), ethanol (a rehydration battery with 100%, 96%, and 80% ethanol for periods of 10 minutes each), and water (both distilled and tap, 10 minutes each), stained with eosin and hematoxylin, and washed with distilled water. Subsequently, the samples were again dehydrated in ethanol (10 minutes) and xylene (10 minutes × 2) baths and mounted for microscopy. The histological study was performed with an OLYMPUS SZX7 dissection microscope and an OLYMPUS BK11 analytical microscope; the captured images were then modified in Adobe Photoshop to regulate the white balance, contrast, and color curves. Finally, to determine the presence of the endogenous digestive bacteria, the deparaffinized histological sections were Gram stained according to the protocol of Kruczak-Filipov and

Shively (1992). The objective was to detect the potential involvement of gut bacteria in the production of biofilms within carcasses (Butler et al., 2015).

To characterize the precipitated chemical elements, the fixed and dehydrated specimens from the microbial mats (i.e., the fifth specimen) were gold coated (thickness = 15 nm) using a Q150T-S Quorum coater and analyzed with a Hitachi S-3000N SEM at the UAM Interdepartmental Research Service. Images were obtained using the secondary electron mode operating at 5 kV, with a 60 μm aperture at a working distance of ~5 mm or using backscatter mode when coupled with the EDXS (energy-dispersive X-ray spectroscopy) analyses, which were performed at 20 kV and a distance of ~15 mm using an Oxford Instruments INCA x-sight analyzer.

The significance of the results was statistically tested based on two data matrices, one focused on the decay (Tables 1 and 2) and the other focused on the biomineralisation process (Table S2). The decay data matrices, qualitatively scored from 0 to 4, were constructed based on the degree of fragmentation and the detachment of the cuticle layers, fat bodies, muscles, digestive tracts, and tracheal networks (Tables 1 and 2) for each period of larval decay. The tissue decay was characterized using the histological transverse sections. The significance of the alterations found was determined using multivariate ordering statistics, including principal component analysis (PCA, using IBM SPSS, Statistics v. 26.0 and R 3.6.3) and the seriation algorithm (Past v. 3.0, Hammer et al., 2001). Partial triadic analysis (PTA), performed with the package for R "ade4" (Dray et al., 2007) was used to explore time-dependent patterns. The elemental composition of the sixty-nine EDXS spectra of the samples was explored relative to the time, location (outside, cuticle and microbial crust, and inside the body), and taxa. Permutational multivariate analysis of variance (PERMANOVA) tests contrasted the significance for each pair of factors (Table S3).

2.4 Cretaceous insects from the Crato Formation

The Crato Formation represents a lacustrine system deposited during the Cretaceous (Aptian) in Brazil, and features laminated limestone, shale, and fine sandstone (Warren et al., 2017). Exposures of the Crato Formation are present in the Araripe Basin, the largest interior basin that resulted from a Jurassic–Cretaceous rifting event in northeastern Brazil (de Matos, 1992; Assine, 2007; Carvalho et al., 2012). The presence of micritic limestones with plane-parallel laminations is often indicative of protected environments, with low benthic activity and gentle bottom currents. The absence of bioturbation associated with the presence of halite pseudomorphs indicates that the lake hypolimnion was possibly hypersaline and hostile for benthic metazoans. Three levels of stromatolites with halite pseudomorphs, oncoids, and wrinkled surfaces suggest that the lacustrine waters were shallow with a significant presence of microbial communities that settled in the stressful environment (Heimhofer and Martill, 2007; Heimhofer et al., 2010; Araújo-Júnior and Carvalho, 2015; Downen et al., 2016; Warren et al., 2017; Varejão et al., 2019). The microbial nature of Crato laminated limestones shows structures that are mediated by microbial production and metabolic activity, such as coccoids, filamentous and acicular cells, and textures linked to the mineralisation of exopolymeric substances (EPS) (Catto et al., 2016).

The diversity of exquisitely preserved fossils, which include algal fragments, woody plants, insects, crustaceans, arachnids, and fish, as well as fully articulated amphibians, chelonians, lizards, dinosaurs, birds, and pterosaurs (Menon and Martill, 2007; Rios-Netto et al., 2012; Carvalho et al., 2019), makes the Crato Formation locality one of the world's best represented Mesozoic palaeobiotic environments (Martill and Bechly, 2007). Using this information, we compare our laboratory decay experiment data with the textural (microfabrics) and chemical (elemental composition and mineralogy) preservation of grylloid fossils from Araripe studied by Osés et al. (2016, 2017) and Dias and Carvalho (2020).

3. Results

3.1 Decay

The monitoring of dead specimens in two types of cultivation chambers (with and without microbial mats) allowed us to determine three major phases of insect larvae. First, bodies floated, primarily because of the internal presence of gas (Peñalver-Mollá, 2002). Larvae floated for 11 ± 3.1 days. Phase two started when bodies finally reached the surface of the sediment (controls) or the microbial mats (Fig. 3 A and B). In the case of controls, this phase was final, and the bodies remained exposed for the rest of the experiment, whereas on the mats, the bodies were progressively covered by the upper layers of the microbial community; phase three entailed the formation of the sarcophagus (Fig. 3 A and B). Complete coverage by the mat was fast and took only 21 ± 2.6 days to fully isolate bodies. MRI showed that the reduction in body volume was more noticeable in *T. molitor* than in *G. mellonella* (Fig. 4 and Fig. S1). The faster compression experienced by the mealworm generated a number of microbreakages and fissures in its exoskeleton (Fig. S2). The MRI protocol enhanced observations of the inner organ contours and hydration of the larva (Fig. 4). The differences between the controls and samples on the mats were not noticeable for *G. mellonella* or *T. molitor* at day 30. However, on day 180, the control larvae were externally and internally decayed and broke during manipulation (Fig. 4). The MRI image of the inner body showed no contrast, and the larvae consisted of a grey mass. However, on day 180, the samples on the mats showed bodily integrity, with visible cuticles and even inner tissues. For example, the digestive tract of *T. molitor* and the silk gland in *G. mellonella* remained discernible (see Fig. 4 and the animated reconstructions in the Audiovisual Supplementary

Material). Interestingly, the MRI allowed for the identification of the mat cover embedding the larvae, which we call the sarcophagus (Fig. 4B).

The decay sequence, tested by serial multivariate analysis using the constrained mode, resulted in a significant non-random process ($p = 8.5 \times 10^{-11}$). The constrained mode found the optimal range plot of the specimens over time according to the scores (0 to 4) of the decayed tissues from the histological sections (Fig. 5, see also Figure S3 for detailed monitoring of the decay of tissues). The larvae of the two species showed the same general patterns in their tissue decay sequences: (a) fat body and muscles decayed early (~day 11); (b) digestive degradation and endogenous bacteria occurred next (~day 30); and (c) the epidermal cuticle and tracheal network were the most perdurable (decaying at days 60 and 120). Notably, the ordering provided by seriation was the same for the control and microbial mat specimens (Fig. 5 A). Observations of tissue damage or the occurrence of bacteria within bodies (presence of squares in the diagram) showed a similar pattern for both species.

The first component of the principal component analysis (PCA) based on the qualitative variables of tissue decay captured 85.66% of the variance and the second up to 7.95% (Fig. 6). The graphic representation of the specimens along the two components showed that (a) Component 1 experienced an increase in decay alterations from the initial stages to the final ones; and (b) the larvae that were decayed in the microbial mats were less dispersed along Component 2, indicating an overall better preservation of all tissues than the controls. Notably, maximal variation occurred between the final measuring times (days 60 to 180) for the control specimens (Fig. 6). This variation reflects the major decay differences between *T. molitor* and *G. mellonella*. The biplot representation of the variables demonstrates that in *G. mellonella* muscles, body fat and digestive tissue tend to resist decay more strongly than the tracheal network and the epidermis, whereas the opposite is true for the mealworm *T. molitor*.

3.1.1 The silk gland in the wax moth

The silk organ showed the best contrast in the MRI sections at days0 and 30 (Fig. 4) due to the large lumen of the middle silk gland (MSG) and the loops filled with a hydrated solution of proteins (fibroin and serine). The histological transverse sections of *G. mellonella* enabled the epithelium of the MSG tracts to be easily identified over experimental time (Fig. 7). The progression of decay in the control was shown by cell disintegration, shedding of the epithelium, and deformation and breakage at day 180 (Fig. 7). The silk glands in the mat remained practically intact until day 120 (Fig. 7 P); on day 180, they were fragmented, albeit to a lesser extent than in the control (Fig. 7 Q–R).

3.1.2 Bacteria from the gut

Bacteria were observed inside the digestive tract mixed with ingested food from days 4–11 (Fig. 8). On day 30, microorganisms appeared in the coelom in the controls of both species. For *G. mellonella* on the mat, the number of bacteria increased more slowly than in the control, and for *T. molitor*, the presence of bacteria was delayed until day 120 (Fig. 8 C and D). The predominant bacterial shape was coccoid or slightly bacillary (1.2–1.5 × 0.9–1.1 µm) in the digestive tract and in the coelom. Most bacterial populations were gram-positive. Furthermore, more elongated (2–4 × 1–1.5 µm), gram-negative, and gram-positive bacillary forms were detected. The number of bacteria inside the bodies increased over time (Fig. 8).

3.2 Biomineralisations

The coverage of the larva by the microbial mat (i.e., the formation of the sarcophagus) occurred faster for *G. mellonella* than for *T. molitor*. At day 4, neither species was fully covered, but both showed an amorphous organic crust covering patchy areas of their external

surface. This crust was made of an organic mesh of EPS and cyanobacteria with enrichment in several mineral elements (Fig. 9). This crust formation favoured the generation of negative impressions of larval segments. The body imprint was especially remarkable for *T. molitor,* whose cuticle was thicker and sclerotised (Fig. 3D). Both species showed very similar crustal compositions dominated by Cl, Na, Mg, and S (Fig. 9 C, D, and G–J) and, occasionally, Ca, P, and K. The atomic percentages of the elements found in the EDXS analysis were likely compatible with a potentially widespread presence of magnesium sulfate and, to a lesser extent, sodium and calcium sulfates and sodium and potassium chloride. Additionally, the presence of Ca detected in the crust was the product of authigenetic precipitation, because calcium was absent in the larvae cuticle, which is composed of chitin and lipids.

The EDXS elemental analysis highlighted an enrichment of the same elements observed in the external crusts inside the body of the two species located in the microbial mat. Some elements, especially S, Mg, and Na, increased over time, especially in *T. molitor*. Additionally, the formation of crystals was different between the mealworm and the wax moth based on observations using SEM (Fig. 10). Although amorphous precipitates or small needles (0.5–2.7 µm) enriched primarily in sodium and calcium sulfate appeared inside the body of *G. mellonella* only over the long-term (Fig. 10 A), *T. molitor* exhibited a great variety of crystal shapes and sizes within its body. Needle-shaped crystals (11.8–35 µm) were observed at day 11, irregular spheres on the inner sides of the cuticles (25–37 µm) appeared on day 30, semi-cubes of sodium and magnesium sulfate in the tracheas (2.2–4.0 µm) appeared at day 120 (Fig. 8 C), and star-shaped crystals that formed via fine needles (12 µm) were observed at day 11. These crystals increased in size until they formed large 79–116-µm stars made of flat sheets of magnesium sulfate at day 180, appearing in bunches that filled the sides of the body during the later decay stages (Fig. 10 B). However, increases in the sizes of the crystals were a frequent observation.

The PERMANOVA test determined that the centroid differences between time, location, and taxa were nearly significant (p-value = 0.07) but had a low coefficient of determination (r^2 = 0.06) (see Table S3 for the tests). The PCA showed that the distribution was time-dependent (earlier–later measurements) and location-dependent (outer–inner bodies), as confirmed using PERMANOVA by combining the factors of "time" and "location" with the cofactor "taxa" (to avoid potential biases due to differences in the taxa) (p-values = 0.02 and 0.05, respectively; see also PTA analysis of the temporal evolution presented in Supp. Fig. S4). The evolution of the elementary composition differed along PC1, which explained 24.06% of the total variability (Fig. 11 A). The samples distributed with positive PC1 values were collected after day 60 and additionally influenced by S and Na (Supplementary Fig. S4 D and E). The correlation between these two elements was consistent with the abundance of sodium sulfate observed by EDXS. Conversely, early samples between days 4–30 were linked with higher concentrations of chloride in the analyses of the outer bodies (negative PC1 values) (also confirmed by PTA, Supplementary Fig. S4 A and B). This early abundance of Cl is consistent with the influence of the original salts present in the system. PCA axis 2 explained 21.03% of the variability and was influenced by the inner content of P and Mg in *T. molitor* (Fig. 11 A and Supplementary Fig. S4 A and B). The early occurrence of precipitates enriched in P and the presence of large crystals of magnesium sulfate in long-term samples mostly occurred in *T. molitor*, as shown in the PERMANOVA test (p-value = 0.06, close to significance; and r^2 = 0.12). *G. mellonella* did not show a significant influence on time and location (p-value = 0.88; r^2 = 0.06). Additionally, we detected that certain elements showed a negative co-occurrence according to Pearson correlation coefficients (Fig. 11 B). For instance, the presence of S, Na, or Mg was associated with K depletion. We also established a positive correlation between Ca and S, which developed after day 60, according to the PTA analysis (Supplementary Fig. S4 D and F).

3.3 Mats and the Crato fossil record.

The grylloid fossils from the Crato Formation are a clear example of exceptional preservation. These remains were articulated and poorly fragmented—many featured three-dimensional preservation—but suffered compaction during diagenesis (Fig. 12). Their body parts (head, thorax, abdomen, and appendages) and soft tissues (compound eyes, digestive tract, ovaries, eggs, and visceral and locomotive muscle tissues) were also preserved (Fig. 12 A-D). Herein, we highlight the microbial features identified in fossilised grylloids that are directly associated with the configuration of a particular microfabric and the primary mineral phases of these fossils.

Fig. 12 H shows the presence of (1) numerous, tiny, equidimensional, spherical grains that are moderately to densely packed, with very similar shapes, isotropic textures, the absence of crystalline faces, and sizes of less than 5 μm; (2) tiny three-dimensional filamentous features of less than 10 μm; and (3) acicular remnants related to the network-shaped texture (1, 2, and 3 in Fig. 12 H). These different shapes are very similar to those observed in the crusts on the larvae in our experiment (Fig. 12 G and I). Moreover, the observed microfabric was rich in carbon (Fig. 13 C) that covered the eye ommatidia and was also present inside the thorax, abdomen, and tegmina (Fig. 12 E).

Fossilised Crato grylloids were potentially preserved in three main mineral phases: (1) iron oxide (structure labelled “2” in Fig. 13 A); (2) carbonaceous materials (Fig. 13 C, D) (in these two cases, replacing the external and internal body structures); and (3) likely calcium phosphate (Fig. 13 A, label 3), which was especially observed in internal soft tissues (see Dias and Carvalho (2020) for a further characterisation of the mineral preservation of these insects). In the iron oxide specimens, the preservation of the cuticle formed a film with a large size and crystals that were difficult to individuate (Fig. 12 B–D), whereas the

microfabric of the inner organs was characterised by subspherical to spherical crystals, euhedral to subhedral crystals, and approximately equidimensional micro- to crypto-crystals, which were easily individualised compared to those in the large outer film (Fig. 12 B, C). The preservation of the carbonaceous specimens was characterised by homogeneous and isotropic materials, featuring a network-shaped texture without evidence of crystal nucleation (Fig. 13 C, D). Finally, phosphatisation was identified in the replication of detailed structures (muscle fibres of the femur and compound eyes) formed by equidimensional crypto-crystals of a mineral rich in Ca and P, likely calcium phosphate.

4. Discussion

This laboratory experiment sheds some light on the decay processes experienced by the larvae of two different insects, *Galleria mellonella* and *Tenebrio molitor*. The decay exposed the sequence of events after dying in an aquatic environment, floating, and resting in the surface of the sediment/microbial mat. Additionally, the presence of microbial mats introduced a third phase: the isolation of the carcass within the sarcophagus by the growth of the upper microbial layers. This experimental design offered the opportunity to compare the decay of different types of tissues using histological features and to trace the synchrony in their decay sequences. The present study also highlighted the differences in inner tissue alterations and mineralisation using distinct and complementary techniques, such as SEM and analytical microscopy. Finally, we compared the experimental results with those of well-documented fossils.

Soft-bodied animals show rapid early decay processes, as previously evidenced in experiments on annelids (Briggs and Kear, 1993), the branchiopod *Artemia* (Butler et al., 2015), and the onychophoran velvet worm (Murdock et al., 2014). In our experiments, the insect larvae resisted longer than in these previous experiments in the control and microbial

mats because of their sclerotised cuticles. Hence, the chronology of their decay was more comparable to that of other biomineralised organisms. The general pattern in all the mentioned soft-bodied invertebrates has the onset of decay starting between days 8 and 15 (in the aftermath of the floating phase), but the most important differences in gross body decay occurred after day 50, and body disarticulation occurred between days 90 and 120. This timeline can be recognised in organisms decayed under open conditions (i.e., in the absence of restricted milieus such as microbial mats), in experiments mediated by microbial veils with arthropods (Hof and Briggs, 1997; Klompmaker et al., 2017), or, particularly, in fossil insects (Peñalver-Mollá, 2002). Nonetheless, the decay rate always varies depending on the origin of the taxa, and the conditions of decay. A clear example of decay rates was outlined by Klompmaker et al. (2017), who studied marine arthropods. Organisms certainly settled in irradiated milieus, and antimicrobial substances, and/or reduced conditions show a retarded decomposition in comparison with those decayed in open control environments (Hof and Briggs, 1997; Butler et al., 2015). The effect of mat entombment (i.e., the isolation of the body within the sarcophagus) yields an equally drastic decay slowdown; the bodies never become fully disarticulated and maintain their integrity for years (Iniesto et al., 2016; see the animated reconstructions presented in the Audiovisual Supplementary Material). Principal component analysis (Fig. 6) confirmed that, in the absence of microbial mats, the larvae in the controls suffered greater decomposition than the other tissues.

Although soft tissue preservation mediated by bacterial precipitation is an observable fact, neither the formation of bacterial replicas nor the autolithification of bacteria were observed over the course of our experiment. Based on experimentation with *Artemia salina* (Crustacea), Butler et al. (2015) described the generation of pseudomorphs by inner digestive microbes, which were able to replicate the shapes of inner tissues over 12 days. During our insect larvae experiments, bacteria were observed, but none met the conditions of experiments

by Butler et al. using *Artemia*. In our assay, we observed that (a) bacteria that penetrated exoskeletal fractures and the aperture of tracheal vestibules might have been exogenous; (b) the time needed to generate pseudomorphs in *Artemia* is too short (12 days) for insect larvae, in which bacteria appeared in the coelom at day 30; (c) most of the organs started to decay once the microorganisms colonised the coelom of the larvae (after day 120)—meaning that cell autolysis (i.e., the initial biochemical decay of tissues independent of bacterial activity, according to Child, 1995 and Clarke et al., 1997) was of little importance during this first period; and (d) the reducing conditions were used to explain the inhibition of autolysis. On the contrary, an oxic environment likely developed inside the larvae decayed within microbial mats (Iniesto et al., 2015). Hence, our data suggest that the observed decay is more strongly related to microbial activity than autolysis, because tissue decay occurred later in the experiment; autolysis is known to be more active soon after death and should be observed during the floating phase (e.g., until day 15–20 in controls).

Interestingly, the decay sequence that occurred in the control and in the mats progressed in the same pattern: fat body → muscles → digestive → epidermis → trachea; fat bodies were the most labile, and trachea were the most resistant. The seriation algorithm, which offers the best enumeration order for a set of described objects, supports the non-random degradation of tissues when the species of both insect orders are compared (Lepidoptera and Coleoptera). This result validates the fundamental observation that decay has a phylogenetic component (Sansom et al., 2010, 2011; Purnell et al., 2018) and that taxonomic decay patterns can be traced as a bias in the fossil record. The sequence we obtained for both insect larvae was different from that described for the mentioned soft bodied organisms, such as the velvet worm —gut → epidermis → nerve → cuticle → gonads → appendages (Murdock et al., 2014)— or annelids —muscle→ gut → cuticle → appendages in annelids (Briggs and Kear, 1993)—. In the insect larvae, the digestive wall, the epidermal

exoskeleton, the silk gland, and the trachea are protected with resistant biomolecules, but there are subtle differences in tissue decay depending on the sclerotisation pattern and the cuticle thickness in the wax moth and mealworm tissues (Fig.7).

4.1 Principal taphonomic features in the decay and mineralisation of the insect larvae

These experiments with microbial mats helped characterise the processes involved in the mineralisation of the insect larvae, which can be compared against data from the insect fossil record produced in lacustrine MISS deposits. The mineralisation of the larvae took place outside the cuticle and in the soft tissues, thereby exhibiting the predominance of sulfate, chloride, and phosphate mineralisation. The Chiprana lacustrine system is rich in magnesium and sulfate ions, chloride, and sodium. The organomineralised crust over the insect cuticle depends on the existence of nucleation centres (Spadafora et al., 2010) and the saturation of these elements, among others. The microbial EPS clearly filled the spaces between the carcasses and the mat layer, acting as chelators for cations (Mg and Ca in our experiment) (Costerton et al., 1995; Trichet and Défarge, 1995; Spadafora et al., 2010). In past experiments using mats and the same organism model for *Galleria mellonella*, a crust was formed by iron sulfides (Darroch et al., 2012). However, Fe was low to absent in our experiment, which explains the absence of these iron sulfides in the crust. This Fe depletion can be explained by the elemental composition present in the system; water and sediments from Chiprana exhibit low concentrations of iron, as shown previously using X-ray diffraction, SEM-EDXS, and inductively coupled plasma atomic emission spectroscopy (ICP-AES) (Iniesto et al., 2015*b*). The crust was enriched in the major elements found in the water (Na, Mg, S, and Cl); in turn, the crust contained Ca and P in variable amounts (Fig. 9).

Sulfurisation is a mineralisation process likely present in inner larvae decay and would explain the substantial S enrichment in of carcass tissues over the course of the experiment.

To understand this process, S-mediated dynamics must be addressed (Hebting et al., 2006). This process, which is considered to be rapid in the early stages of decay, is favoured in our system because of the large quantity of sulfates present in the water and the release of sulfates during the decay of the bodies (desulfurisation). Sulfurisation of organic matter is frequent in systems where the inputs of bacterially generated sulfide exceed the availability of reactive iron (Sinninghe Damsté et al., 1993; Briggs, 2003). In our experiments, this process can be promoted by the abundance of sulfate in the water column and the scarcity of iron, whose presence is not required for sulfurisation (Sinninghe Damsté et al., 1993; Melendez et al., 2012). Although certain organic molecules are predisposed to sulfurisation during early diagenesis (Melendez et al., 2012), we have not tested the actual incorporation of inorganic sulfur in organic matter, which was not observed over the course of our experiment and requires further study.

T. molitor larvae showed an interesting mineralisation process with enrichment in Na and Mg, compaction of tissues, and progressive detachment of soft tissues from the cuticle (Fig. 10 A, B). The enrichment of Mg is related to muscle decay (Briggs, 2003; Newman et al., 2019) and could also be linked to sulfurisation promoted by bacterial activity (McNamara et al., 2016). Nonetheless, although the organs within the compacted soft tissues (the tracheal orifices, muscle, and digestive walls) could be clearly recognised up to day 180; the digestive walls were evident, and the tissues appeared obscured due to the appearance of precipitated crystals. The blurring of the internal organs was enhanced by the large void spaces at day 180, where the crystals occupied the entire gap. These crystals filled the empty spaces of the larva, destroying the remains of the tissues. This appearance of minerals was also favoured by the fractures observed in the cuticle of *T. molitor*, which allowed the passage of water and solutes that promoted the formation of precipitates within the carcass, as suggested for Cretaceous fossil insects from the Crato Formation (Osés et al., 2016).

4.2 From laboratory experiment to the fossil record

A clear parallel can be traced between this experiment and Crato fossils when comparing the textures and elemental composition of the organomineralised crust and the web-like fossil microfabric. The organic and amorphous crust covering the outer surface of the wax moth and mealworm larvae can be compared to the massive external film with poorly individualised crystals found in the upper layer of the MISS sediment. In fact, the mineralised crusts of extracellular polymeric substances (EPS) in the experiment (Fig. 12G) mimic the network-shaped texture (Fig. 12C and 13D), acicular remains (Fig. 12H), and carbon location in the fossils (Fig. 13C).

Delicate features are evident in the Crato grylloid fossils, such as spines, sensilla, antennae, and soft tissues, including muscles, digestive tracts, and ovaries. The preservation of these tissues seems to be ubiquitous among insect fossils (Delclòs et al., 2004; Osés et al., 2016). The digestive tract was also identified as a resistant organ. In the Crato insects, anatomical microstructures associated with a highly sclerotised region formed by cuticular structures and denticles (i.e., the lining of the proventriculus) were recognised in the digestive tract (Dias and Carvalho, 2020). The cuticle that forms part of the anterior and posterior digestive wall is composed of chitin, which is a polysaccharide that forms a hard coating (Gooday, 1990). This organic molecule has high potential for preservation (Flannery et al., 2001; Gupta, 2011; Iniesto et al., 2019), increasing the time in which the digestive tract can maintain its integrity. However, preservation controversial, as chitin is often preserved only as remnants inside geopolymers (Cody et al., 2011).

Crato Grylloidea is classified based on three types of fossilisation processes: pyritisation, phosphatisation, and kerogenisation (Dias and Carvalho, 2020). Experiments with insect larvae performed for 180 days showed the initial phases (Purnell et al., 2018) of

the maturation process, which can be related to early sulfurisation that can take place in a few days (Raven et al., 2016) and is likely favoured by a specific set of environmental conditions: in saline waters as a photochemically induced reaction, in shallow water tanks, and in organisms that are rich in lipids because of the presence of extraordinary reservoirs of fat bodies in the insect larvae (Kok et al., 2000; Werne et al., 2004). Additionally, sulfurisation is frequent in saline lakes with sulfur- and gypsum-rich waters, such as the famous fossils of the lacustrine settings of Libros and Rubielos de Mora (Miocene, Teruel, Spain) (McNamara et al., 2016; Purnell et al., 2018). Furthermore, this mode of exceptional preservation may be transformed into large aliphatic chains (kerogenisation), exhibiting carbonaceous layers that could occur on the surface of an organism or its tissues (e.g., the kerogenised Crato grylloids (Dias and Carvalho, 2020) and Jehol carbonaceous-compressed ephemeropteran larvae (Pan et al., 2014) are good examples of this). Other mineralisations, such as pyritisation and phosphatisation, likely depend on the concentration of ions inside the sarcophagus created by the microbial mats; the formation of sufficient fissures in the insect cuticle would likely promote the input of solutes, thereby facilitating mineralisation of the external cuticle and inner soft tissues (Osés et al., 2016, 2017).

5. Conclusions

Analytical approaches are necessary to understand the complexity of soft tissue decay in animals placed in cultivation chambers with and without microbial mats. Fossilisation assisted by microbial mats has been suggested as a key factor in exceptional deposits, and the present study provides experimental credibility to the relevance of mats in fossilisation. The results are supported by data from 96 soft-bodied wax moth (Lepidoptera) larvae and mealworm (Coleoptera) insects. The larvae floated for ~11 days and then rested on the surface of the sediment (controls) or were progressively embedded in the mat (full coverage occurred ~day

30). The alteration patterns were sustained by the details observed in histological thin sections, which offered new features to characterisecharacteris the chronology of the decay processes. The pattern of decay indicates a non-random process that occurred with the same sequence in the mats and in the control chambers, starting with fat body and muscles, continuing with the digestive presence of endogenous bacteria and the epidermal cuticle, and ending with sclerotised organs (i.e., the silk glands or tracheal networks). We also found that histological sections might be relevant in differentiating decay in distinct phylogenetic lineages in future experiments. The mineralisation process is characterischaracterised by the substantial enrichment in sulfur in larvae tissues, which could be related to early sulfurisation. S enrichment is congruent with a set of environmental conditions, such as saline waters, shallowness of water, and the inherent properties of the larvae, which are rich in lipids. Additionally, the evidence provided by our experiment with lepidopteran and coleopteran larvae help us better understand the ways in which the body and organs can be preserved in fossils. Our comparison with grylloids from the Crato Formation shows that the pattern of preservation and the presence of soft tissue in those fossils is potentially consistent with the presence of microbial mats. These outcomes are of great interest, because larvae are abundant in the fossil record in different Mesozoic localities, such as Jehol (Pan et al., 2014) and the Crato Formation (Storari et al., 2019), whose fossils were produced in lacustrine environments with microbial mats. Additional taphonomic experiments similar to this one, using actual mats and monitoring their influence on the decay pattern, can have a valuable impact for producing data that help interpret the formation of numerous Konservat-Lagerstätten.

FUNDING AND ACKNOWLEDGMENTS

This work is part of the research projects CGL2013-42643-P (concluded) and PID2019-105546GB-I00 (in progress) funded by the Spanish Ministry of Science and Innovation. The research contract supporting MI was funded by the French ANR "Microbialites" (ANR-18-CE02-0013-01; PI: López-García, P). Part of the financial support was also provided by the Fundação Carlos Chagas Filho de Amparo à Pesquisa do Estado do Rio de Janeiro (FAPERJ) and Conselho Nacional de Desenvolvimento Científico e Tecnológico (CNPq). We thank Luiz C. Bertolino of Setor de Caracterização Tecnológica (CETEM) from Rio de Janeiro/Brazil for the help with microscopic studies on SEM-EDXS. We also thank the three anonymous reviewers who performed a thorough revision and helped us to improve substantially our initial manuscript, and also the Elsevier language editing service for the detailed language revision.

REFERENCES

Alleon, J., Bernard, S., Le Guillou, C., Daval, D., Skouri-Panet, F., Pont, S., Delbes, L., Robert, F., 2016. Early entombment within silica minimizes the molecular degradation of microorganisms during advanced diagenesis. Chem. Geol. 437, 98–108. https://doi.org/10.1016/j.chemgeo.2016.05.034

Andersson, M., Johansson, J., Rising, A., 2016. Silk spinning in silkworms and spiders. Int. J. Mol. Sci. https://doi.org/10.3390/ijms17081290

Araújo-Júnior, H., Carvalho, I., 2015. Variação na salinidade do paleolago Crato (Aptiano da Formação Santana, Bacia do Araripe) com base na tafonomia de aranhas fósseis, in: XIV Simpósio De Geologia Do Sudeste/VIII Simpósio Do Cretáceo Do Brasil. p. 122.

Assine, M., 2007. Bacia do Araripe. Bol. Geociências da Petrobrás 12, 371–389.

Bernard, S., Benzerara, K., Beyssac, O., Menguy, N., Guyot, F., Brown Jr, G.E., Goffé, B., 2007. Exceptional preservation of fossil plant spores in high-pressure metamorphic rocks. Earth Planet. Sci. Lett. 262, 257–272. https://doi.org/10.1016/j.epsl.2007.07.041

Borror, D.J., Triplehorn, C.A., Johnson, N.F., 1989. An introduction to the study of insects. Saunders College Pub, Chicago.

Briggs, D.E.G., 2003. The role of decay and mineralisation in the preservation of soft-bodied fossils. Annu. Rev. Earth Planet. Sci. 31, 275–301. https://doi.org/10.1146/annurev.earth.31.100901.144746

Briggs, D.E.G., Kear, A.J., 1993. Fossilisation of soft tissue in the laboratory. Science 259, 1439–42. https://doi.org/10.1126/science.259.5100.1439

Briggs, D.E.G., McMahon, S., 2016. The role of experiments in investigating the taphonomy of exceptional preservation. Palaeontology 59, 1–11. https://doi.org/10.1111/pala.12219

Briggs, D.E.G., Wilby, P.R., 1996. The role of the calcium carbonate-calcium phosphate switch in the mineralisation of soft-bodied fossils. J. Geol. Soc. London. 153, 665–668.

Butler, A.D., Cunningham, J.A., Budd, G.E., Donoghue, P.C.J., 2015. Experimental taphonomy of *Artemia* reveals the role of endogenous microbes in mediating decay and fossilisation. Proc. Biol. Sci. 282, 20150476. https://doi.org/10.1098/rspb.2015.0476

Button, D., Unwin, D.M., Purnell, M., 2012. Continuous character states and their impact on the phylogeny of the Pterosauria. J. Vertebr. Paleontol. 32, 72nd Annual Meeting of the Society of Vertebrate P.

Carvalho, I., Agnolin, F., Rolando, M., Novas, F., Xavier-Neto, J., Freitas, F., Andrade, J., 2019. A new genus of pipimorph frog (anura) from the early Cretaceous Crato Formation (Aptian) and the evolution of South American tongueless frogs. J. South Am. Earth Sci. 92, 222–233.

Carvalho, I., Freitas, F., Neumann, V., 2012. Chapada do Araripe, in: Hasui, Y., Carneiro, C., Almeida, F., Bartorelli, A. (Eds.), Geologia Do Brasil. BECA, São Paulo, pp. 510–513.

Catto, B., Jahnert, R.J., Warren, L.V., Varejao, F.G., Assine, M.L., 2016. The microbial nature of laminated limestones: Lessons from the upper Aptian, Araripe Basin, Brazil. Sediment. Geol. 341, 304–315. https://doi.org/10.1016/j.sedgeo.2016.05.007

Channing, A., Edwards, D., 2004. Experimental taphonomy: Silicification of plants in Yellowstone hot-spring environments. Trans. R. Soc. Edinburgh, Earth Sci. 94, 503–521. https://doi.org/10.1017/s0263593300000845

Child, A. M., 1995. Microbial taphonomy of archaeological bone. Studies in Conservation 40, 19–30 doi:10.2307/1506608

Clark, M.A., Worrell, M.B., Pless, J. E., 1997. Chapter 9: Postmortem changes in soft tissues. , in: Haglund, W.D., Sorg, M.H. (Eds.), Forensic taphonomy: the postmortem fate of human remains. CRC Press, London, pp. 151–164.

Cody, G.D., Gupta, N.S., Briggs, D.E., Kilcoyne, A.L.D., Summons, R.E., Kenig, F., Plotnick, R.E., Scott, A.C., 2011. Molecular signature of chitin-protein complex in Paleozoic arthropods. Geology 39(3), 255-258

Costerton, J.W., Lewandowski, Z., Caldwell, D.E., Korber, D.R., Lappin-Scott, H.M., 1995. Microbial biofilms. Annu. Rev. Microbiol. 49, 711–45. https://doi.org/10.1146/annurev.mi.49.100195.003431

Darroch, S.A.F., Laflamme, M., Schiffbauer, J.D., Briggs, D.E.G., 2012. Experimental formation of a microbial death mask. Palaios 27, 293–303. https://doi.org/10.2110/palo.2011.p11-059r

de Matos, R.M.D., 1992. The Northeast Brazilian Rift System. Tectonics 11, 766–791. https://doi.org/10.1029/91TC03092

De Wit, R., 2016. Lake la Salada de Chiprana (NE Spain), an example of an athalassic salt lake in a cultural landscape, in: Rashed, M.N. (Ed.), Lake Sciences and Climate Change. IntechOpen. https://doi.org/10.5772/64443

Delclòs, X.M., Briggs, D.E.G., Peñalver-Mollá, E., 2004. Taphonomy of insects in carbonates and amber. Palaeogeogr. Palaeoclimatol. Palaeoecol. 203, 19–64. https://doi.org/10.1016/S0031-0182(03)00643-6

Delclòs, X.M., Soriano, C., 2016. Insecta, in: Poyato-Ariza, F.J., Buscalioni, A.D. (Eds.), Las Hoyas: A Cretaceous Wetland. A Multidisciplinary Synthesis after 25 Years of Research on an Exceptional Fossil Lagerstätte from Spain. Verlag Dr. Friedrich Pfeil, München, pp. 70–88.

Dias, J.J., Carvalho, I. de S., 2020. Remarkable fossil crickets preservation from Crato Formation (Aptian, Araripe Basin), a Lagerstätten from Brazil. J. South Am. Earth Sci. 98, 102443. https://doi.org/10.1016/j.jsames.2019.102443

Downen, M.R., Selden, P.A., Hasiotis, S.T., 2016. Spider leg flexure as an indicator for estimating salinity in lacustrine paleoenvironments. Palaeogeogr. Palaeoclimatol. Palaeoecol. 445, 115–123. https://doi.org/10.1016/j.palaeo.2015.11.028

Dray, S., Dufour, A., Chessel, D., 2007. The ade4 Package – II: Two-Table and K-Table Methods. R News 7, 47–52. https://cran.r-project.org/doc/Rnews/.

Emery, H., Johnston, R., Rowley, A.F., Coates, C.J., 2019. Indomethacin-induced gut damage in a surrogate insect model, *Galleria mellonella*. Arch. Toxicol. 93, 2347–2360. https://doi.org/10.1007/s00204-019-02508-4

Flannery, M.B., Stott, A.W., Briggs, D.E.G., Evershed, R.P., 2001. Chitin in the fossil record: Identification and quantification of D-glucosamine. Org. Geochem. 32, 745–754. https://doi.org/10.1016/S0146-6380(00)00174-1

Fourçans, A., de Oteyza, T.G., Wieland, A., Solé, A., Diestra, E., van Bleijswijk, J., Grimalt, J.O., Kühl, M., Esteve, I., Muyzer, G., Caumette, P., Duran, R., 2004. Characterization of functional bacterial groups in a hypersaline microbial mat community (Salins-de-Giraud, Camargue, France). FEMS Microbiol. Ecol. 51, 55–70. https://doi.org/10.1016/j.femsec.2004.07.012

Gäb, F., Ballhaus, C., Stinnesbeck, E., Kral, A.G., Janssen, K, Bierbaum, G., 2020. Experimental taphonomy of fish - role of elevated pressure, salinity and pH. Sci. Rep. 10(1), 7839 doi:10.1038/s41598-020-64651-8

Gehling, J.G., 1999. Microbial mats in terminal proterozoic siliciclastics: ediacaran death masks. Palaios 14, 40. https://doi.org/10.2307/3515360

Gooday, G.W., 1990. The ecology of chitin degradation. Adv. Microb. Ecol. 11, 387–430. https://doi.org/10.1007/978-1-4684-7612-5_10

Grimm, J., Potthast, A., Wunder, A., Moore, A., 2003. Magnetic resonance imaging of the pancreas and pancreatic tumors in a mouse orthotopic model of human cancer. Int. J. Cancer 106, 806–811. https://doi.org/10.1002/ijc.11281

Gupta, N.S., 2010. Chitin: formation and diagenesis. Springer Netherlands, Houten. https://doi.org/10.1007/978-90-481-9684-5

Hajek, A.E., St. Leger, R.J., 1994. Interactions between fungal pathogens and insect hosts. Annu. Rev. Entomol. 39, 293–322. https://doi.org/10.1146/annurev.en.39.010194.001453

Hammer, Ø., Harper, D.A.T., Ryan, P.D., 2001. PAST: Paleontological Statistics Software package for Education. Palaeontol. Electron.

Hebting, Y., Schaeffer, P., Behrens, A., Adam, P., Schmitt, G., Schneckenburger, P., Bernasconi, S.M., Albrecht, P., 2006. Biomarker evidence for a major preservation pathway of sedimentary organic carbon. Science 312, 1627–1631. https://doi.org/10.1126/science.1126372

Heimhofer, U., Ariztegui, D., Lenniger, M., Hesselbo, S.P., Martill, D.M., Rios-Netto, A.M., 2010. Deciphering the depositional environment of the laminated Crato fossil beds (Early Cretaceous, Araripe Basin, north-eastern Brazil). Sedimentology 57, 677–694. https://doi.org/10.1111/j.1365-3091.2009.01114.x

Heimhofer, U., Martill, D.M., 2007. The sedimentology and depositional environment of the Crato Formation, in: Martill, D., Bechly, G., Loveridge, R. (Eds.), The Crato Fossil Beds of Brazil. Cambridge University Press, Cambridge, pp. 44–62.

Hof, C.H.J., Briggs, D.E.G., 1997. Decay and mineralisation of mantis shrimps (Stomatopoda; Crustacea); a key to their fossil record. Palaios 12, 420–438. https://doi.org/10.1043/0883-1351(1997)012<0420:DAMOMS>2.0.CO;2

Hoshizaki, D.K., 2013. The insects: structure and function, 5th ed. Cambridge University Press, Cambridge.

Iniesto, M., Blanco-Moreno, C., Villalba, A., Buscalioni, Á., Guerrero, M., López-Archilla, A., 2018. Plant tissue decay in long-term experiments with microbial mats. Geosciences 8, 387. https://doi.org/10.3390/geosciences8110387

Iniesto, M., Buscalioni, Á.D., Guerrero, M.C., Benzerara, K., Moreira, D., López-Archilla, A.I., 2016. Involvement of microbial mats in early fossilisation by decay delay and formation of impressions and replicas of vertebrates and invertebrates. Sci. Rep. 6, 1–12. https://doi.org/doi:10.1038/srep25716

Iniesto, M., Laguna, C., Florín, M., Carmen Guerrero, M., Chicote, A., Buscalioni, A.D., López-Archilla, A.I., 2015a. The impact of microbial mats and their microenvironmental conditions in early decay of fish. Palaios 30. https://doi.org/10.2110/palo.2014.086

Iniesto, M., Lopez-Archilla, A.I., Fregenal-Martínez, M., Buscalioni, A.D., Carmen Guerrero, M., 2013. Involvement of microbial mats in delayed decay: An experimental essay on fish preservation. Palaios 28. https://doi.org/10.2110/palo.2011.p11-099r

Iniesto, M., Thomazo, C., Fara, E., Bylund, K.G., Escarguel, G., Goudemand, N., Guériau, P., Jenks, J.F., Krumenacker, L.J., Olivier, N., Stephen, D.A., Thoury, M., Vennin, E., Brayard, A., 2019. Deciphering the exceptional preservation of the Early Triassic Paris Biota (Bear Lake County, Idaho, USA). Geobios 54, 81–93. https://doi.org/10.1016/j.geobios.2019.04.002

Iniesto, M., Villalba, I., Buscalioni, A.D., Guerrero, M.C., López-Archilla, A.I., 2017. The effect of microbial mats in the decay of anurans with implications for understanding taphonomic processes in the fossil record. Sci. Rep. 7, 45160. https://doi.org/10.1038/srep45160

Iniesto, M., Zeyen, N., López-Archilla, A.I., Bernard, S., Buscalioni, Á.D., Guerrero, M.C., Benzerara, K., 2015b. Preservation in microbial mats: Mineralisation by a talc-like phase of a fish embedded in a microbial sarcophagus. Front. Earth Sci. 3. https://doi.org/10.3389/feart.2015.00051

Jacquemot, P., Viennet, J.C., Bernard, S., Le Guillou, C., Rigaud, B., Delbes, L., Georgelin, T., Jaber, M., 2019. The degradation of organic compounds impacts the crystallisation of clay minerals and viceversa. Sci. Rep. 9, 1–6. https://doi.org/10.1038/s41598-019-56756-6

Jonkers, H.M., Ludwig, R., de Wit, R., Pringault, O., Muyzer, G., Niemann, H., Finke, N., de Beer, D., 2003. Structural and functional analysis of a microbial mat ecosystem from a unique permanent hypersaline inland lake: "La Salada de Chiprana" (NE Spain). FEMS Microbiol. Ecol. 44, 175–189.

King, B., Denholm, B., 2014. Malpighian tubule development in the red flour beetle (*Tribolium castaneum*). Arthropod Struct. Dev. 43, 605–613. https://doi.org/10.1016/j.asd.2014.08.002

Klompmaker, A.A., Portell, R.W., Frick, M.G., 2017. Comparative experimental taphonomy of eight marine arthropods indicates distinct differences in preservation potential. Palaeontology 60, 773–794. https://doi.org/10.1111/pala.12314

Kludkiewicz, B., Kucerova, L., Konikova, T., Strnad, H., Hradilova, M., Zaloudikova, A., Sehadova, H., Konik, P., Sehnal, F., Zurovec, M., 2019. The expansion of genes encoding soluble silk components in the greater wax moth, *Galleria mellonella*. Insect Biochem. Mol. Biol. 106, 28–38. https://doi.org/10.1016/j.ibmb.2018.11.003

Kok, M.D., Schouten, S., Sinninghe Damsté, J.S., 2000. Formation of insoluble, nonhydrolyzable, sulfur-rich macromolecules via incorporation of inorganic sulfur species into algal carbohydrates. Geochim. Cosmochim. Acta 64, 2689–2699. https://doi.org/10.1016/S0016-7037(00)00382-3

Kong, H.G., Kim, H.H., Chung, J. Hui, Jun, J.H., Lee, S., Kim, H.M., Jeon, S., Park, S.G., Bhak, J., Ryu, C.M., 2019. The *Galleria mellonella* Hologenome supports microbiota-independent metabolism of long-chain hydrocarbon beeswax. Cell Rep. 26, 2451–2464.e5. https://doi.org/10.1016/j.celrep.2019.02.018

Kruczak-Filipov, P., Shively, R., 1992. Gram stain procedure, in: Isenberg, H. (Ed.), Clinical Microbiology Procedures Handbook. American Society for Microbiology, Washington DC.

Li, J., Bernard, S., Benzerara, K., Beyssac, O., Allard, T., Cosmidis, J., & Moussou, J. (2014). Impact of biomineralisation on the preservation of microorganisms during fossilisation: An experimental perspective. Earth and Planetary Science Letters 400, 113-122.

Martill, D.M., Bechly, G., 2007. Introduction to the Crato Formation, in: Martill, D.M., Bechly, G., Loveridge, R.F. (Eds.), The Crato Fossils Beds of Brazil. Cambridge University Press, Cambridge, pp. 3–7.

McNamara, M.E., van Dongen, B.E., Lockyer, N.P., Bull, I.D., Orr, P.J., 2016. Fossilisation of melanosomes via sulfurization. Palaeontology 59, 337–350. https://doi.org/10.1111/pala.12238

Melendez, I., Grice, K., Trinajstic, K., Ladjavardi, M., Greenwood, P., Thompson, K., 2012. Biomarkers reveal the role of photic zone euxinia in exceptional fossil preservation: An organic geochemical perspective. Geology 41, 123–126. https://doi.org/10.1130/G33492.1

Menon, F., Martill, D.M., 2007. Taphonomy and preservation of Crato Formation arthropods, in: Martill, D., Bechly, G., Loveridge, R. (Eds.), The Crato Fossil Beds of Brazil. Cambridge University Press, Cambridge, pp. 79–96.

Montigon, O., 2006. https://irmage.ujf-grenoble.fr/accueil.

Morales-Ramos, J.A., Rojas, M.G., Shapiro-Ilan, D.I., Tedders, W.L., 2010. Developmental Plasticity in *Tenebrio molitor* (Coleoptera: Tenebrionidae): Analysis of Instar Variation in Number and Development Time under Different Diets. J. Entomol. Sci. 45, 75–90. https://doi.org/10.18474/0749-8004-45.2.75

Murdock, D.J.E., Gabbott, S.E., Mayer, G., Purnell, M.A., 2014. Decay of velvet worms (Onychophora), and bias in the fossil record of lobopodians. BMC Evol. Biol. 14, 222. https://doi.org/10.1186/s12862-014-0222-z

Murdock, D.J.E., Gabbott, S.E., Purnell, M.A., 2016. The impact of taphonomic data on phylogenetic resolution: *Helenodora inopinata* (Carboniferous, Mazon Creek Lagerstätte) and the onychophoran stem lineage. BMC Evol. Biol. 16, 19. https://doi.org/10.1186/s12862-016-0582-7

Neville, A., 1975. Biology of the arthropod cuticle. Springer-Verlag Berlin Heidelberg, Heidelberg.

Newman, S.A., Daye, M., Fakra, S.C., Marcus, M.A., Pajusalu, M., Pruss, S.B., Smith, E.F., Bosak, T., 2019. Experimental preservation of muscle tissue in quartz sand and kaolinite. Palaios 34, 437–451. https://doi.org/10.2110/palo.2019.030

Noffke, N., Awramik, S.M., 2013. Stromatolites and MISS—Differences between relatives. GSA Today 23, 4–9.

Noffke, N., Gerdes, G., Klenke, T., Krumbein, W.E., 2001. Perspectives microbially induced sedimentary structures — A new category within the classification of primary sedimentary structures. J. Sediment. Res. 71, 649–656.

Novelline, R., 2004. Squire's fundamentals of radiology, 6th ed. Harvard University Press, Cambridge.

Osés, G.L., Petri, S., Becker-Kerber, B., Romero, G.R., Rizzutto, M. de A., Rodrigues, F., Galante, D., da Silva, T.F., Curado, J.F., Rangel, E.C., Ribeiro, R.P., Pacheco, M.L.A.F., 2016. Deciphering the preservation of fossil insects: A case study from the Crato Member, Early Cretaceous of Brazil. PeerJ 2016, e2756. https://doi.org/10.7717/peerj.2756

Osés, G.L., Petri, S., Voltani, C.G., Prado, G.M.E.M., Galante, D., Rizzutto, M.A., Rudnitzki, I.D., Da Silva, E.P., Rodrigues, F., Rangel, E.C., Sucerquia, P.A., Pacheco, M.L.A.F., 2017. Deciphering pyritization-kerogenization gradient for fish soft-tissue preservation. Sci. Rep. 7, 1–15. https://doi.org/10.1038/s41598-017-01563-0

Pan, Y., Sha, J., Fürsich, F., 2014. A model for organic fossilisation of the Early Cretaceous Jehol Lagerstätte based on the taphonomy of *Ephemeropsis trisetalis.* Palaios 29, 363–377. https://doi.org/10.2110/palo.2013.119

Park, J. Bin, Choi, W.H., Kim, S.H., Jin, H.J., Han, Y.S., Lee, Y.S., Kim, N.J., 2014. Developmental characteristics of *Tenebrio molitor* larvae (Coleoptera: Tenebrionidae) in different instars. Int. J. Ind. Entomol. 28, 5–9. https://doi.org/10.7852/ijie.2014.28.1.5

Pebet, N., 2004. Resonancia nuclear magnética, in: XIII Seminario de Ing. Biomédica 2004 Monografıa Vinculada a La Conferencia Del Ing. Rafael Sanguinetti Sobre Radiologıa Sin Pelıcula: Una Puesta Al Dıa de Las Caracterısticas de Proyecto de Sistemas PACS (Picture Archiving and Communication System). Univ. de la República Oriental del Uruguay, Montevideo.

Peñalver-Mollá, E., 2002. Los insectos dípteros del Mioceno del Este de la Península Ibérica; Rubielos de Mora, Ribesalbes y Bicorp. Tafonomía y sistemática. Universitat de València.

Pereira, M.F., Rossi, C.C., de Queiroz, M.V., Martins, G.F., Isaac, C., Bossé, J.T., Li, Y., Wren, B.W., Terra, V.S., Cuccui, J., Langford, P.R., Bazzolli, D.M.S., 2015. *Galleria mellonella* is an effective model to study *Actinobacillus pleuropneumoniae* infection. Microbiol. (United Kingdom) 161, 387–400. https://doi.org/10.1099/mic.0.083923-0

Purnell, M.A., Donoghue, P.J.C., Gabbott, S.E., McNamara, M.E., Murdock, D.J.E., Sansom, R.S., 2018. Experimental analysis of soft-tissue fossilisation: opening the black box. Palaeontology 61, 317–323. https://doi.org/10.1111/pala.12360

Raś, M., Iwan, D., Kamiński, M.J., 2018. The tracheal system in post-embryonic development of holometabolous insects: a case study using the mealworm beetle. J. Anat. 232, 997–1015. https://doi.org/10.1111/joa.12808

Raven, M. R., Sessions, A. L., Adkins, J. F., & Thunell, R. C. (2016). Rapid organic matter sulfurization in sinking particles from the Cariaco Basin water column. Geochimica et Cosmochimica Acta 190, 175-190.

Riches, S.F., Payne, G.S., Morgan, V.A., Sandhu, S., Fisher, C., Germuska, M., Collins, D.J., Thompson, A., Desouza, N.M., 2009. MRI in the detection of prostate cancer: Combined apparent diffusion coefficient, metabolite ratio, and vascular parameters. Am. J. Roentgenol. 193, 1583–1591. https://doi.org/10.2214/AJR.09.2540

Rios-Netto, A., Regali, M., Carvalho, I., Freitas, F., 2012. Palinoestratigrafia do intervalo Alagoas da Bacia do Araripe, Nordeste do Brasil. Rev. Bras. Geociências 42, 331–342.

Roberts, P.E., Willis, J.H., 1980. The cuticular proteins of Tenebrio molitor. I. Electrophoretic banding patterns during postembryonic development. Dev. Biol. 75, 59–69. https://doi.org/10.1016/0012-1606(80)90143-8

Sagemann, J., Bale, S.J., Briggs, D.E.G., Parkes, R.J., 1999. Controls on the formation of authigenic minerals in association with decaying organic matter : An experimental approach. Geochim. Cosmochim. Acta 63, 1083–1095.

Sansom, R.S., 2014. Experimental decay of soft tissues, in: Laflamme, M., Schiffbauer, J.D., Darroch, S.A. (Eds.), Reading and writing of the fossil record: preservational pathways to exceptional fossilisation. The Paleontological Society Papers, Volume 20. The Paleontological Society, Cambridge, pp. 259-274

Sansom, R.S., Gabbott, S.E., Purnell, M.A., 2011. Decay of vertebrate characters in hagfish and lamprey (Cyclostomata) and the implications for the vertebrate fossil record. Proc. Biol. Sci. 278, 1150–7. https://doi.org/10.1098/rspb.2010.1641

Sansom, R.S., Gabbott, S.E., Purnell, M.A., 2010. Non-random decay of chordate characters causes bias in fossil interpretation. Nature 463, 797–800. https://doi.org/10.1038/nature08745

Schindelin, J., Arganda-Carreras, I., Frise, E., Kaynig, V., Longair, M., Pietzsch, T., Preibisch, S., Rueden, C., Saalfeld, S., Schmid, B., Tinevez, J.Y., White, D.J., Hartenstein, V., Eliceiri, K., Tomancak, P., Cardona, A., 2012. Fiji: An open-source platform for biological-image analysis. Nat. Methods. https://doi.org/10.1038/nmeth.2019

Sinninghe Damsté, J.S., de las Heras, F.X.C., van Bergen, P.F., de Leeuw, J.W., 1993. Characterization of Tertiary Catalan lacustrine oil shales: Discovery of extremely organic

sulphur-rich Type I kerogens. Geochim. Cosmochim. Acta 57, 389–415. https://doi.org/10.1016/0016-7037(93)90439-4

Slater, T. S., McNamara, M. E., Orr, P. J., Foley, T. B., Ito, S., & Wakamatsu, K. (2020). Taphonomic experiments resolve controls on the preservation of melanosomes and keratinous tissues in feathers. Palaeontology 63(1), 103-115. https://doi.org/10.1111/pala.12445

Smith, T.L., 1965. External morphology of the larva, pupa, and adult of the wax moth, *Galleria mellonella* L. J. Kansas Entomol. Soc. https://doi.org/10.2307/25083456

Spadafora, A., Perri, E., Mckenzie, J.A., Vasconcelos, C., 2010. Microbial biomineralisation processes forming modern Ca:Mg carbonate stromatolites. Sedimentology 57, 27–40. https://doi.org/10.1111/j.1365-3091.2009.01083.x

Stal, L.J. (2012) Cyanobacterial Mats and Stromatolites, in: Whitton B. (Ed.), Ecology of Cyanobacteria II. Springer, Dordrecht. https://doi.org/10.1007/978-94-007-3855-3_4

Storari, A., Salles, F., Saraiva, A., Rodrigues, T., 2019. New specimens of Hexagenitidae (Ephemeroptera) from the Crato Formation (Aptian, Lower Cretaceous), Brazil, in: 2nd Palaeontological Virtual Congress. Palaeontological Virtual Congress.

Trichet, J., Défarge, C., 1995. Non-biologically supported organomineralisation. Inst. Ocean. Bull. 14, 203–236.

Varejão, F.G., Warren, L. V., Simões, M.G., Fürsich, F.T., Matos, S.A., Assine, M.L., 2019. Exceptional preservation of soft tissues by microbial entombment: insights into the taphonomy of the Crato Konservat-Lagerstätte. Palaios 34, 331–348. https://doi.org/10.2110/palo.2019.041

Vigneron, A., Jehan, C., Rigaud, T., Moret, Y., 2019. Immune Defenses of a Beneficial Pest: The Mealworm Beetle, Tenebrio molitor. Front. Physiol. 10: 138. https://doi.org/10.3389/fphys.2019.00138

Warren, L.V., Varejão, F.G., Quaglio, F., Simões, M.G., Fürsich, F.T., Poiré, D.G., Catto, B., Assine, M.L., 2017. Stromatolites from the Aptian Crato Formation, a hypersaline lake system in the Araripe Basin, northeastern Brazil. Facies 63, 1–19. https://doi.org/10.1007/s10347-016-0484-6

Werne, J.P., Hollander, D.J., Lyons, T.W., Sinninghe Damsté, J.S., 2004. Organic sulfur biogeochemistry: Recent advances and future research directions, in: Amend, J., Edwards, K., Lyons, T. (Eds.), Sulfur biogeochemistry—Past and present. Geological Society of America, Boulder, pp. 135–150.

FIGURE CAPTIONS

Fig. 1. A) Geographic location of Lake La Salada de Chiprana (Aragón) in the NE of Spain and a satellite view of the lake (source: Google Maps). Samples were collected at the shore (white arrow, GPS coordinates 41°14'21.2"N 0°11'11.2"W). B) Microbial mats from the shore presented a characteristic honeycomb pattern (pinnacles) of the microbial mat surface. C) Section of the mat showing the upper layer dominated by cyanobacteria (green layer, gl) and the lower layers dominated by red anoxygenic photosynthetic bacteria (red layer, rl) above the sediments (s).

Fig. 2. Schematic drawings of the external morphology and inner anatomy of the larva *Galleria mellonella* (A) and *Tenebrio molitor* (B). The blue color of the body corresponds with thicker sclerotized zones of the cuticle. The internal structures shown (tracheal network highlighted in red, the digestive tract in green, and the fat bodies in yellow) are present in both insects (only shown in *T. molitor*), except for the silk gland (absent in *T. molitor*).

Abbreviations: Fgut, foregut or estomodeum; HGut, hindgut or proctodeum; Mgut, midgut or mesenteron; MSG, medium silk gland; PSG, posterior silk gland; a1–a5, numbering of the first abdominal segments. Drawing based on our histological observations and Smith (1965), Neville (1975), and Borror et al. (1989).

Fig. 3: Gross morphology and features of the insect larvae. A) Specimens ordered by time of *G. mellonella* on the mat; note the coverage of the bodies. B) Specimens of the same species in control cultivation chambers. C) Organomineral crust (mat sarcophagus, white arrow) and negative impression of the head of *T. molitor* at day 180. D) Impression of the body segments of *T. molitor* at the inner lamina of the sarcophagus (white arrow). E) Dissection of *T. molitor* and the inner organs exposed ventrally. F) Detail of the posterior part of *T. molitor*'s digestive anatomy and the surrounding organs from a ventral view. G) and H) Dissection of *G. mellonella* showing the disposition of the internal organs from a ventral view. Abbreviations: ANT: anterior part of the body; cu, cuticle; d, day; dt, digestive tract; fb, fat bodies; he, head; mt, Malpighi tubules; sg, silk glands; t, trachea. Scale bars: A and B, 20 mm; C, 2 mm; D, 2 mm; E, 10 mm; F. 5 mm; G, 2 mm; H, 0.5 mm.

Fig. 4: Magnetic Resonance Imaging (MRI) of *G. mellonella*. A) Superimposed contours of the body to show the volume loss when using 3D reconstructions at days 0, 30, and 180 (see also Figure S1). B) Two-dimensional images of *G. mellonella* larvae in the mat at day 30 (top) and at day 180 (middle). The bottom image is a 3D reconstruction based on different MRI sections. Abbreviations: c, control; GM, *G. mellonella*; m, mat; mc microbial crust; s, sediment; sg, silk gland. Scale bars = 10 mm.

Fig. 5: A) Seriation multivariate shows the temporal sequence of decay observed during the course of the experiment in both species. The sequence details the evolution of the decay of tissuesover time, and the presence of bacteria in the coelom in TM (*T mollitor*) and GM (*G. mellonella*). For each characteristic monitored, the occurrence of a square indicates a modification in relation with the original state (e.g., decay or occurrence of bacteria). The discontinuous series (i.e., the digestive tract in *G. mellonella* or the presence of bacteria within the coelom in *T. molitor*) are due to variability across individuals. B) Light microscope images of histological sections of the anterior abdominal segments (see also Figure S3 for detailed monitoring of the decay of tissues). Abbreviations: C, control; cu, cuticle; fb, fatty bodies; mp, muscle packs; L: laying on the surface; M: microbial mat; sg, silk glands; t, trachea. Scale bar 50µm

Fig. 6. Temporal and spatial evolution of the elemental composition in the course of the experiment. A) Principal component analysis showing the distribution of the decayed tissues according the decay scores in *T. molitor* (TM) and *G. mellonella* (GM) in the control (C) and mat conditions (M) over time. The variable biplots are shown in the graphic. B) Graphical representation of the Pearson correlation coefficient.

Fig. 7. Histological sections of specimens from the control and mat cultivation chambers stained with eosin and hematoxylin. A–I) *T. molitor*. J–R) *G.mellonella*. Time of experimentation (T) given in days. Abbreviations: cu, cuticle; fb, fatty bodies; mp, muscle packs; pl, proleg; sg, silk gland; t, trachea. Scale bars: B–I = 0.5 mm; K–R = 0,5 mm. The white arrow points to the digestive tract of *T. molitor* and the silk gland of *G. mellonella*.

Fig. 8. Bacteria inside *T. molitor*. A) Optical microscope image of Gram staining of the bacteria confined within the digestive tract of the larva in the mat at day 30. B) Optical microscope image of the bacteria inside and outside the digestive tract of the larva in the sediment (control) at day 30. C) SEM image of the bacteria on the trachea at 120 days. D) SEM image of the bacteria in the coelom at 120 days. Arrows point to groups of bacteria. Abbreviations: c, coelom; dt, digestive tract. Scale bars: A–C = 20 µm; D = 10 µm.

Fig. 9. SEM images of transverse sections. External organomineral crust formed at the top of the head of *G. mellonella* (A) and *T. molitor* (E) taken at day 4. B and F correspond to magnifications of the spots highlighted in A and E respectively, which were analyzed with EDXS. C) Area and elemental spectra within the crust. D) Area and elemental spectra outside the crust in *G. mellonella*. F) Location of the areas (G–I) analyzed in *T. molitor*. Note the presence of some filaments of cyanobacteria. G) Elemental composition of the crust. H) Analysis of the spherical precipitate. I) Analysis of the original cuticle composition. Scale bars: A and E, = 1 mm; B and F= 100 µm.

Fig. 10. SEM images of the bioprecipitates located inside the larval body. A) Transversal section of *G. mellonella* at day 180 (scale bar = 1 mm. B) Magnification of the spot highlighted by the white circle in A. The shape of a large crystal cluster is made of small needles of 0.5–3.0 µm is shown. C) EDXS elemental composition of the needle pointed to by the arrow corresponds to sulfates (enriched in sodium and/or calcium). D) Transversal section of *T. molitor* at day 180. The white circle shows the area magnified in E. E) Star-shaped crystals formed from flat sheets. F) EDXS showing the flat sheets in E consistent with the presence of magnesium sulfates. G) Transversal section of *T. molitor* at day 11. H) The crystals highlighted in G are small in size (the needles are 11 to 35 µm in size), and the

elemental composition (I) is consistent with the occurrence of sodium and magnesium sulfates. The cuticle and the void spaces in A and D are shaped with a dotted line in orange. Abbreviations**:** c, cuticle; mp, muscle pack; t, trachea; v, void spaces.

Fig. 11. Evolution of the elemental composition over time and per waxmoth and mealworm: (A) PCA based on elemental composition using EDXS. The negative values of PC1 correspond to the elements that are mostly precipitated during early phases of decay and tested outside the larval body. B) Graphical representation of the correlation matrix of these elements.

Fig. 12: A) Anatomical features of exquisitely preserved fossil insects of the Grylloidea superfamily recognized in the laminated limestone of the Crato Formation, Aptian, Brazil. B) External cuticle (ct) preserved in the form of a large film with difficult individualization of its crystals and associated internal parts. C) Detail of the grylloid's microfabric displayed in E with the micro- and cryptocrystals approximately equidimensional. D) Lateral view of Grylloidea in SEM, with the external cuticle replaced by a massive film. E) Polygonal facets of one of the compound eyes of a Grylloidea covered by the network texture (nt), a structure associated with the mineralisation of extracellular polymeric substances (EPSs). F) Portion of the digestive tract with associated denticles and microvilli (indicated by arrows). These morphological features are responsible for breaking down food and absorbing nutrients during food digestion. G) SEM image of the crust formed by EPS and microorganisms on the head of *G. mellonella* at 120 days. H) Microfabric with numerous spherical equidimensional grains interpreted as coccoids detected within the abdomen of the grylloid. I) External organomineral crust with bacteria of different forms embedded in an EPS matrix on the head of *G. mellonella* at day 180. 1) coccoid bacteria, 2) bacterial filaments, and 3) long and fine bacteria (acicular).

Fig. 13: A) Chemical analysis of the EDXS of the grylloid's posterior femur showing that the massive external cuticle (2) is replaced by iron oxide, while the associated internal muscle fibers (3) have a primary composition of P and Ca, corresponding to calcium phosphate. The presence of Ca in the matrix (1) is associated with the calcium carbonate of the laminated limestone. B) Detail of the muscle fibers (indicated by the arrows) displayed in A, with replication of their structures by densely packed cryptocrystals of calcium phosphate. C) Abdominal region of a grylloid with the cuticle replaced by a grayish black material. Chemical analyses of EDXS point to the carbonaceous composition of the fossil, with no direct association with Fe, as shown in A. D) Detail of the internal portions of the fossil displayed in C, with the presence of a network texture without individualization of the crystals. Abbreviations**:** O, oxyge□; Fe, iro□; Ca, calcium; P, pho□phoru□; C, carbo□.


Gijón
Oviedo
La Coruña
Bilbao
Vitoria
Vigo
Valladolid
Zaragoza
Barcelona
Madrid
Valencia
Palma
de Mallorca
Alicante
Murcia
Córdoba
Sevilla
Granada
Málaga
Las Palmas
de Gran Canaria
150 km
100 mi
© d-maps.com


A
N
Laguna Salada
41°14'34N
41°14'16N
100 m
0°11'18W
0°10'42W

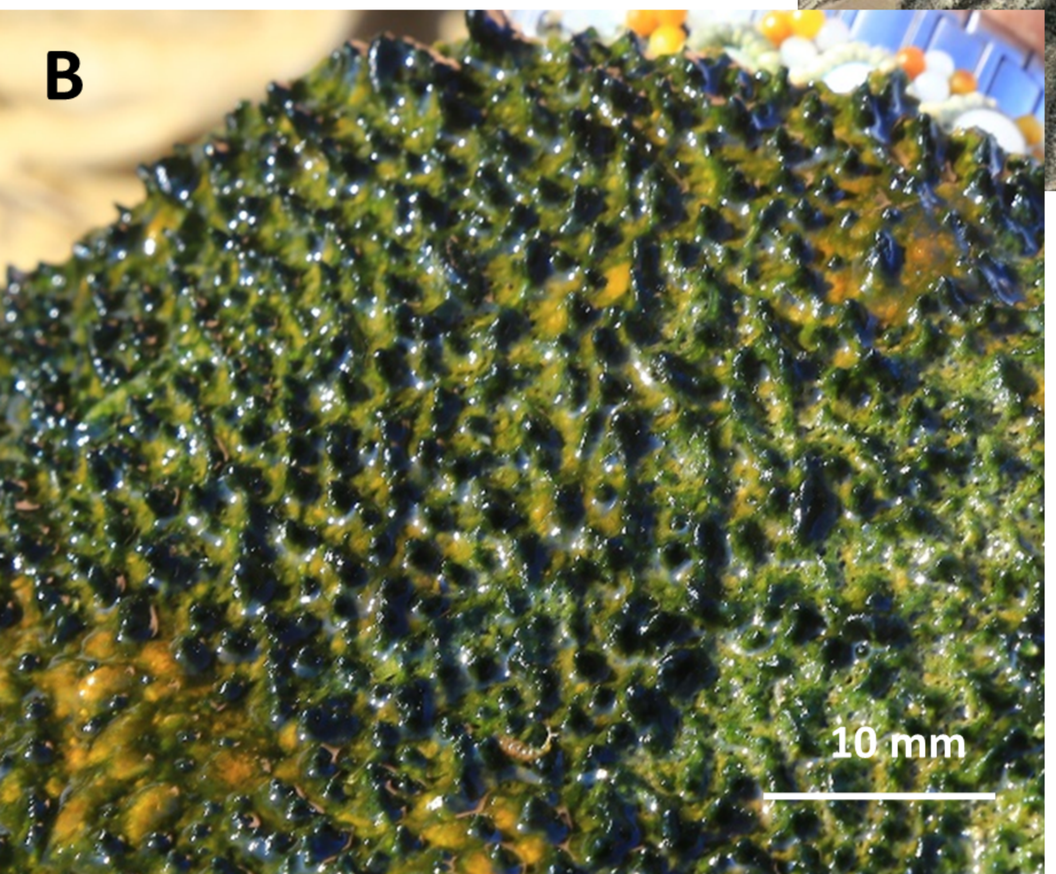
B
10 mm

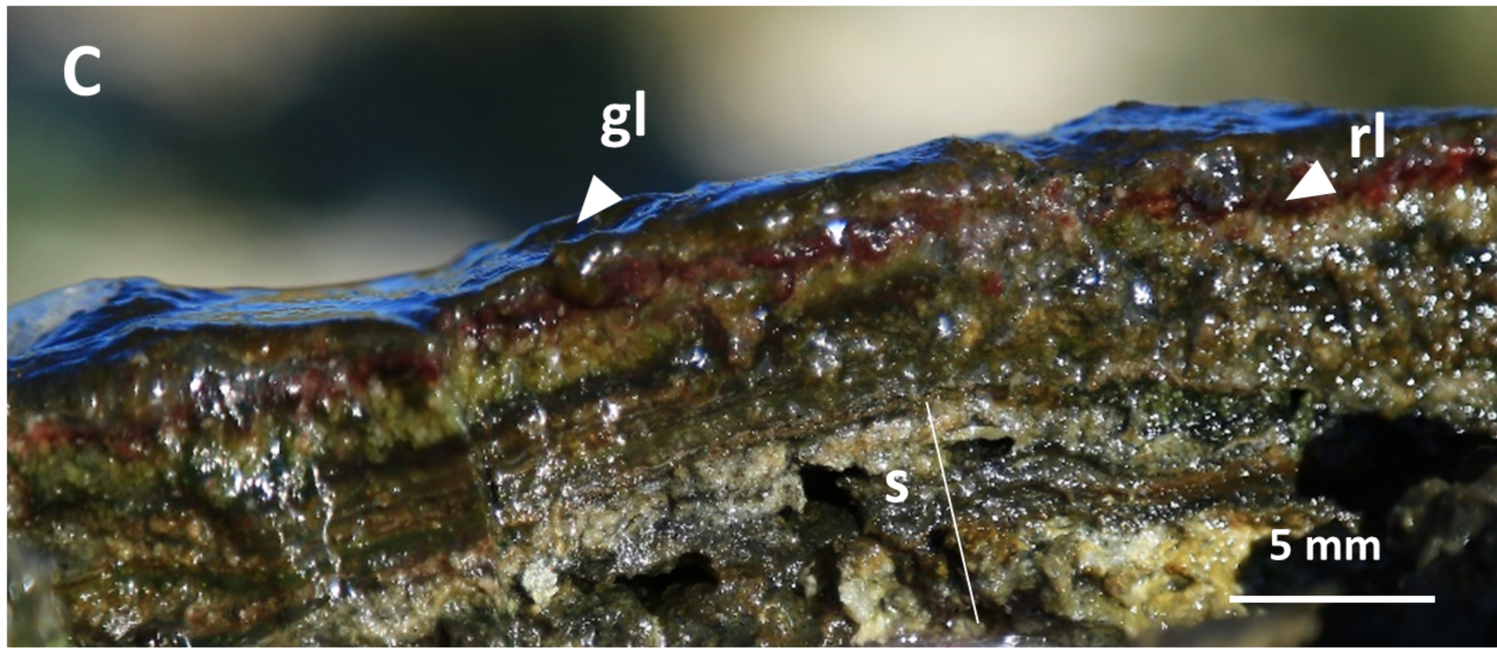
C
gl
rl
s
5 mm

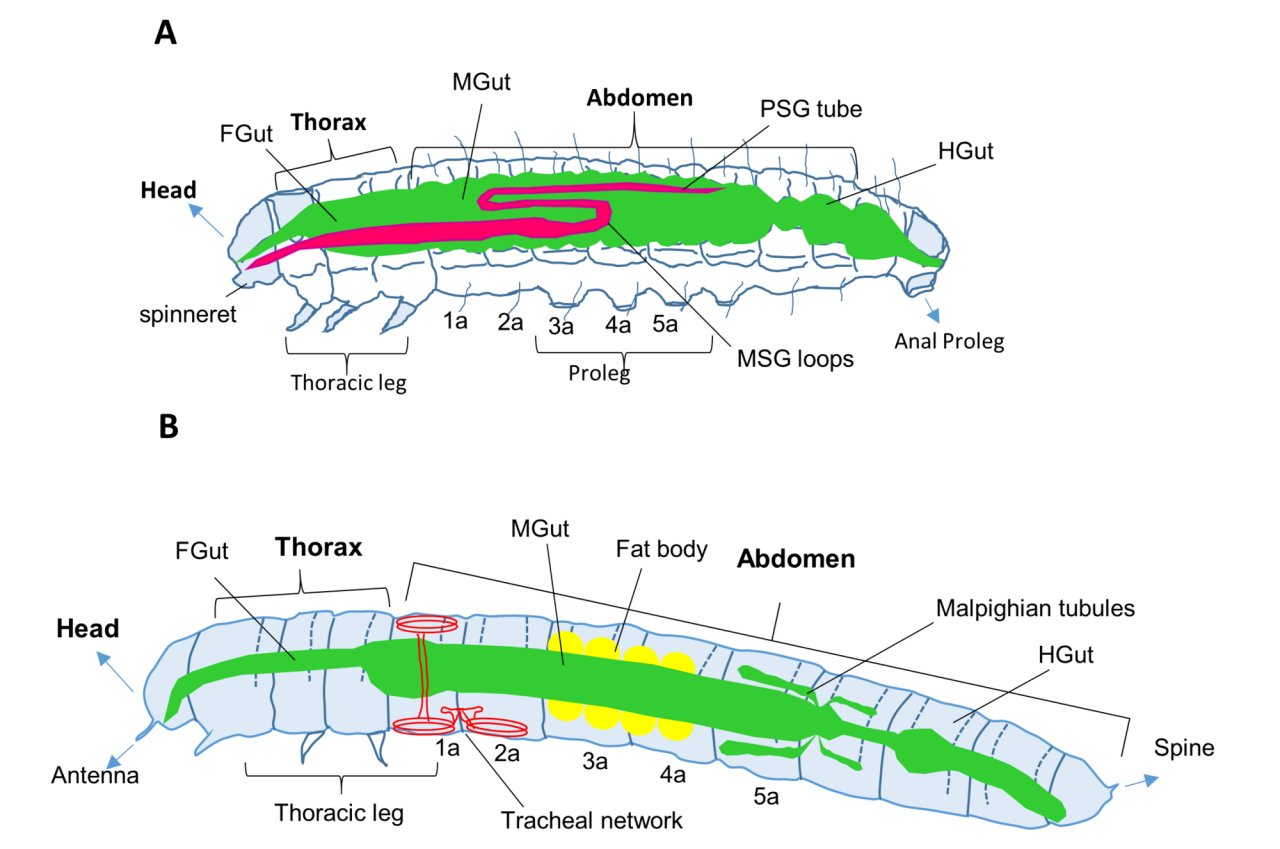
A
MGut
Abdomen
PSG tube
FGut
Thorax
HGut
Head
spinneret
1a
2a
3a
4a
5a
Anal Proleg
MSG loops
Thoracic leg
Proleg
B
FGut
Thorax
MGut
Fat body
Abdomen
Malpighian tubules
Head
HGut
Spine
Antenna
1a
2a
3a
4a
5a
Thoracic leg
Tracheal network

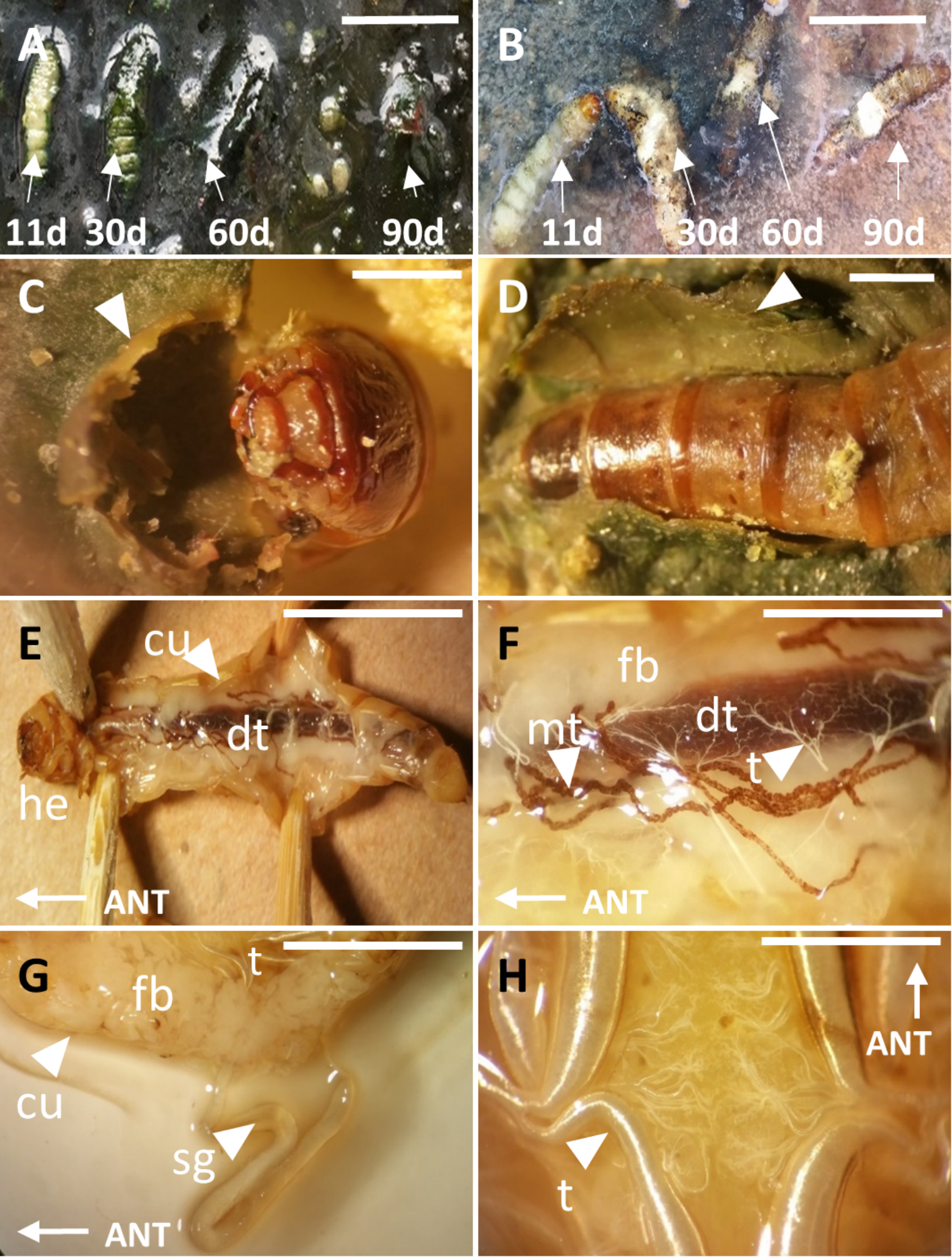
A
11d
30d
60d
90d
B
11d
30d
60d
90d
C
D
E
cu
dt
he
ANT
F
fb
mt
dt
t
ANT
G
t
fb
cu
sg
ANT
H
ANT
t

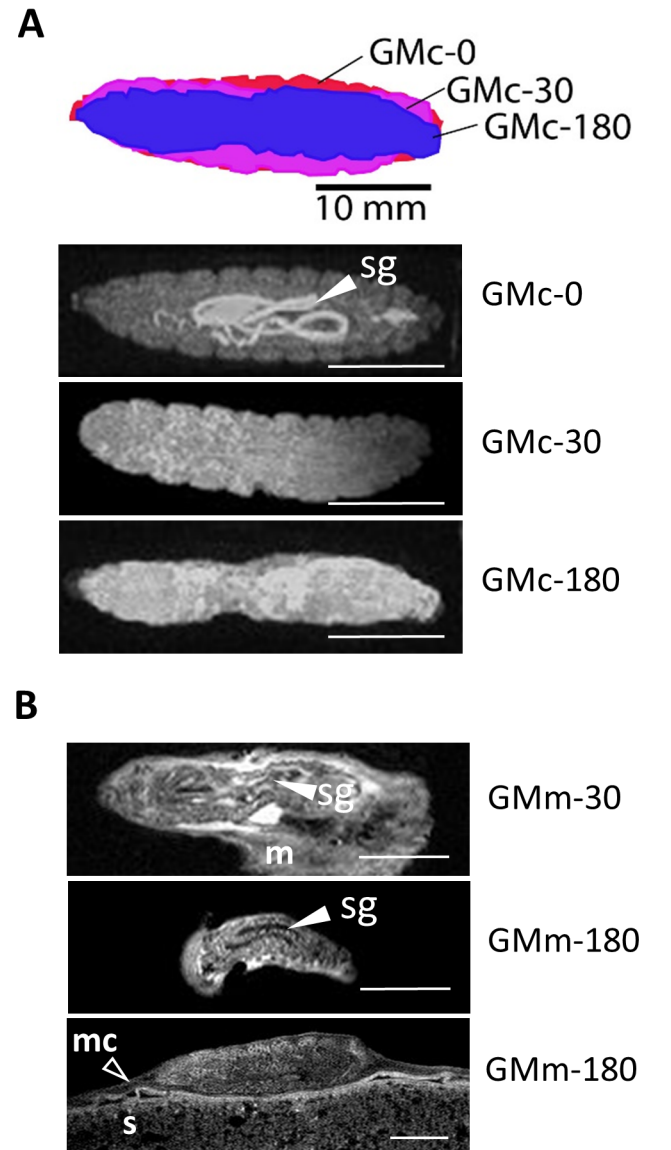
A
GMc-0
GMc-30
GMc-180
10 mm
sg
GMc-0
GMc-30
GMc-180
B
sg
m
GMm-30
sg
GMm-180
mc
s
GMm-180

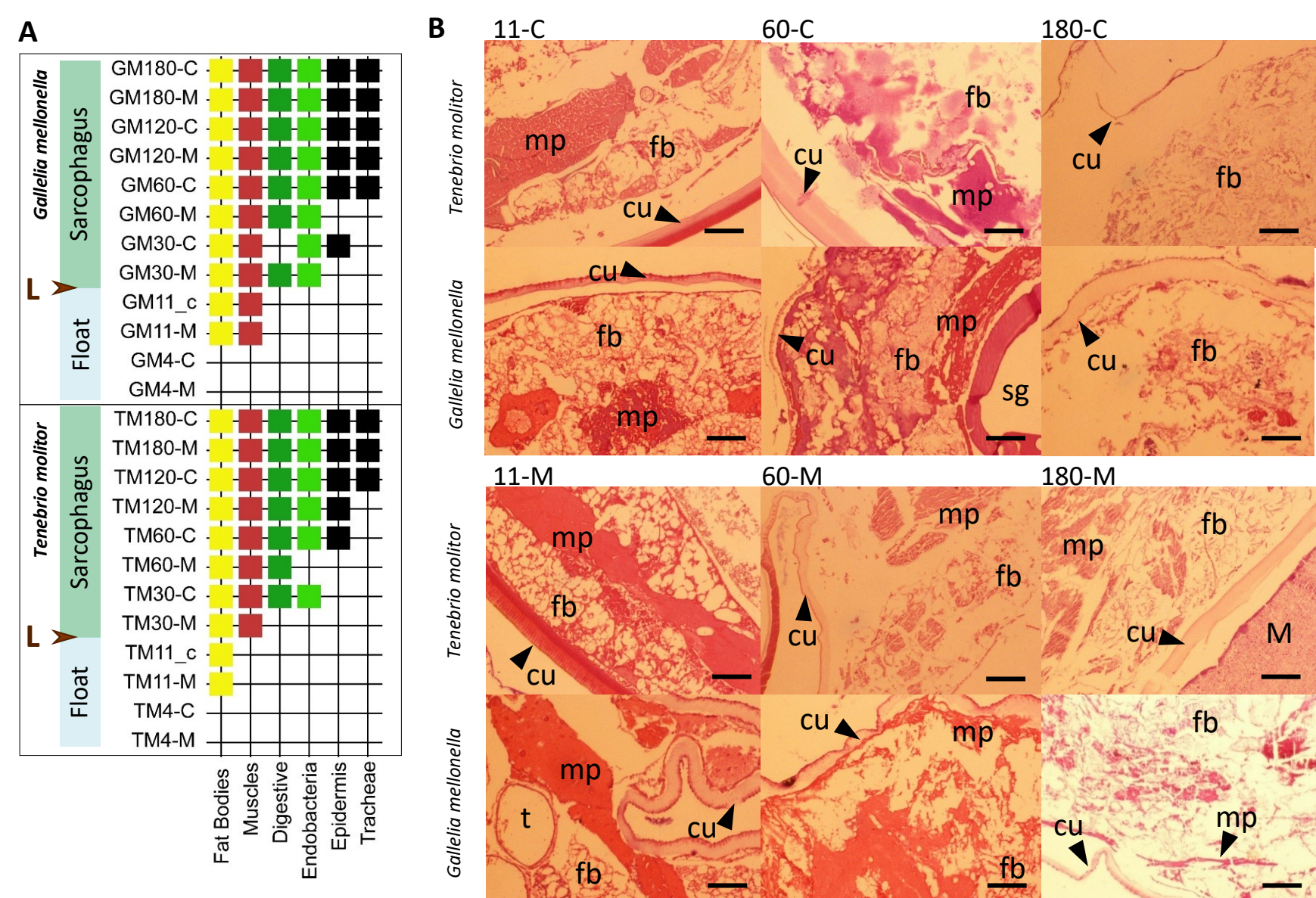
A
Gallelia mellonella
Sarcophagus
Float
L
GM180-C
GM180-M
GM120-C
GM120-M
GM60-C
GM60-M
GM30-C
GM30-M
GM11_c
GM11-M
GM4-C
GM4-M
Tenebrio molitor
Sarcophagus
Float
L
TM180-C
TM180-M
TM120-C
TM120-M
TM60-C
TM60-M
TM30-C
TM30-M
TM11_c
TM11-M
TM4-C
TM4-M
Fat Bodies
Muscles
Digestive
Endobacteria
Epidermis
Tracheae
B
11-C
60-C
180-C
11-M
60-M
180-M
Tenebrio molitor
Gallelia mellonella
mp
fb
cu
sg
M
t

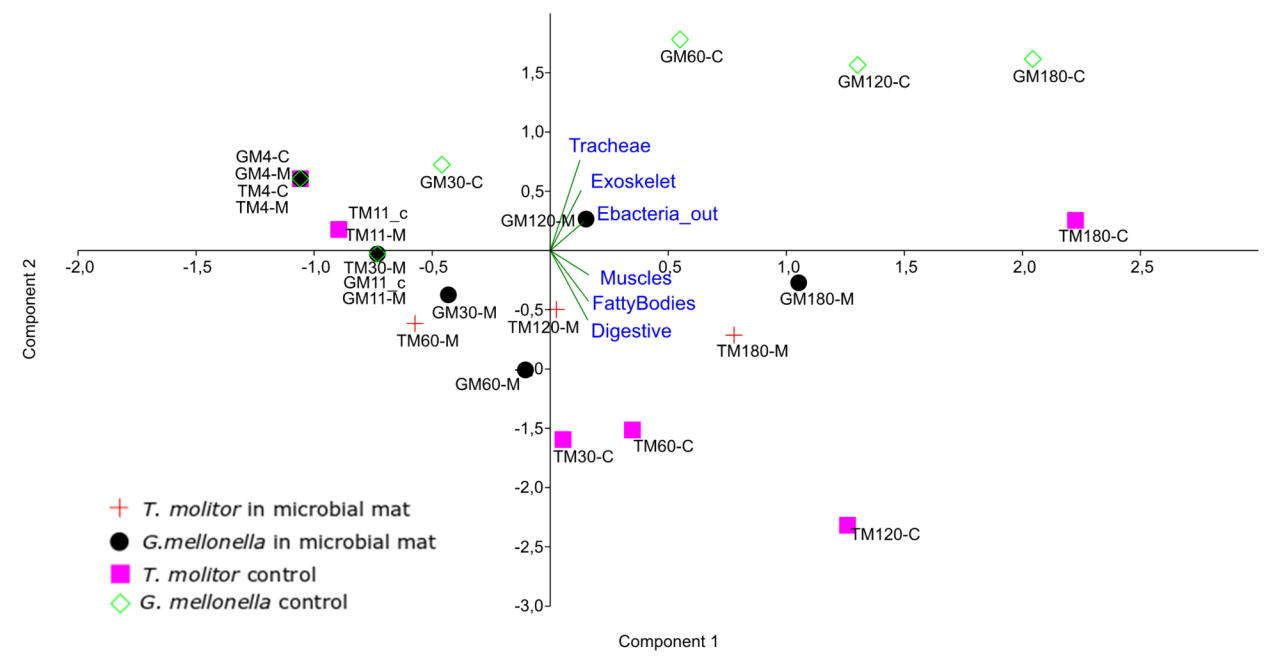
GM60-C
GM120-C
GM180-C
GM4-C
GM4-M
TM4-C
TM4-M
GM30-C
TM11_c
TM11-M
GM120-M
Tracheae
Exoskelet
Ebacteria_out
TM180-C
TM30-M
GM11_c
GM11-M
GM30-M
TM60-M
TM120-M
Muscles
FattyBodies
Digestive
GM180-M
TM180-M
GM60-M
TM30-C
TM60-C
TM120-C
T. molitor in microbial mat
G.mellonella in microbial mat
T. molitor control
G. mellonella control
Component 1
Component 2
1,5
1,0
0,5
0
-0,5
-1,5
-2,0
-2,5
-3,0
-2,0
-1,5
-1,0
-0,5
0,5
1,0
1,5
2,0
2,5

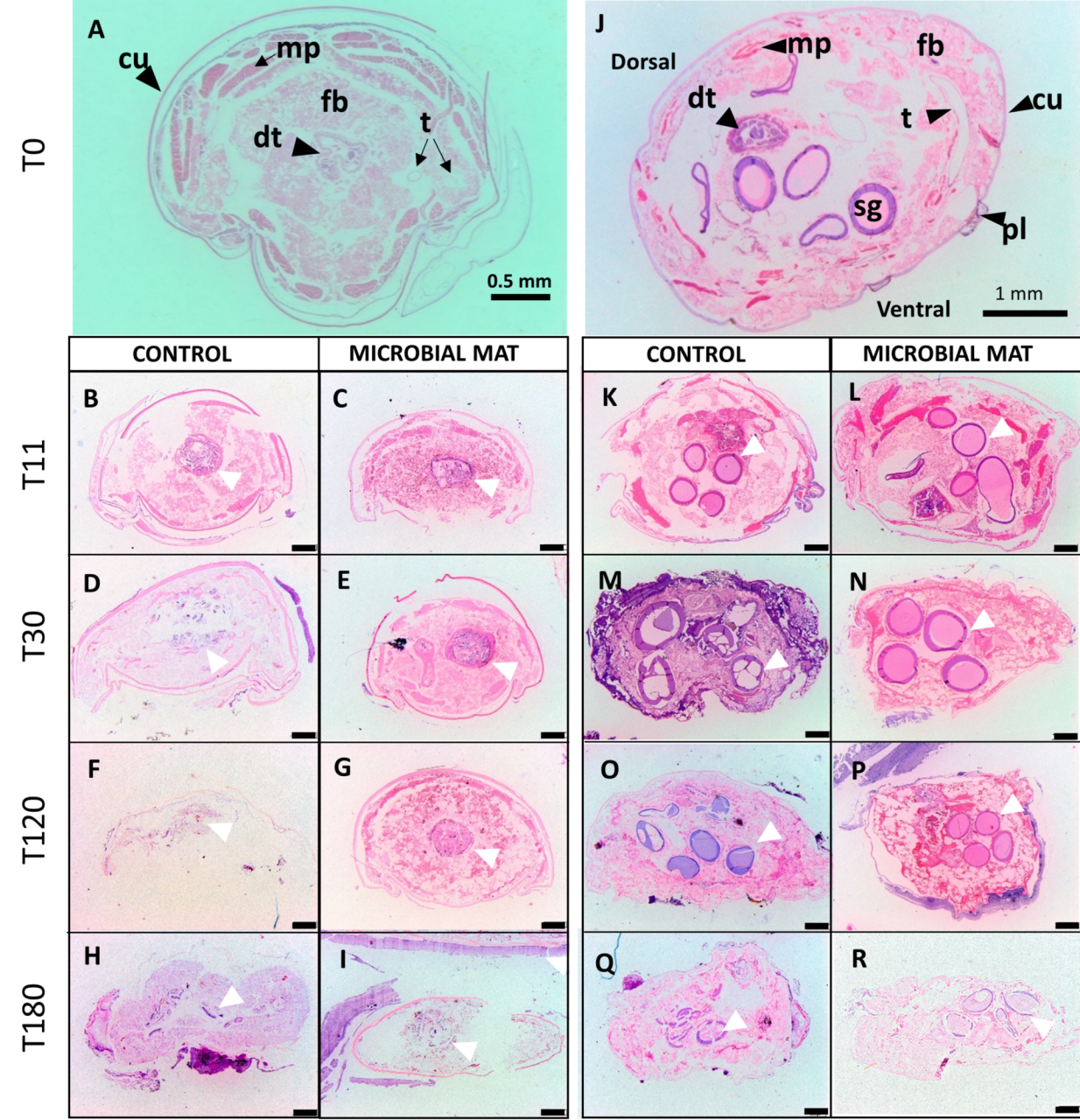
T0
A
cu
mp
fb
dt
t
0.5 mm
J
Dorsal
mp
fb
dt
t
cu
sg
pl
Ventral
1 mm
CONTROL
MICROBIAL MAT
CONTROL
MICROBIAL MAT
T11
B
C
K
L
T30
D
E
M
N
T120
F
G
O
P
T180
H
I
Q
R

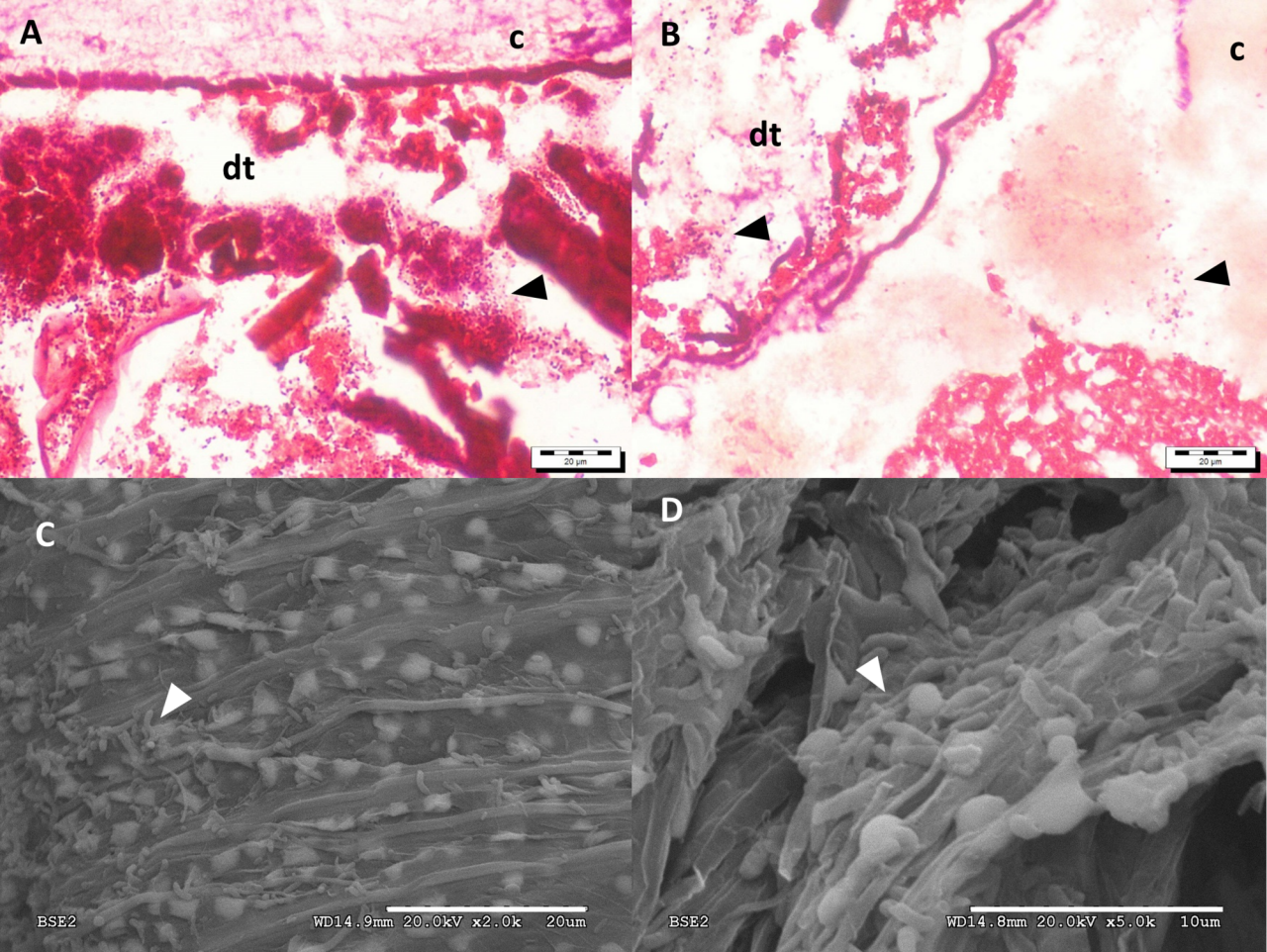
A
c
dt
20 µm
B
c
dt
20 µm
C
BSE2
WD14.9mm 20.0kV x2.0k 20um
D
BSE2
WD14.8mm 20.0kV x5.0k 10um

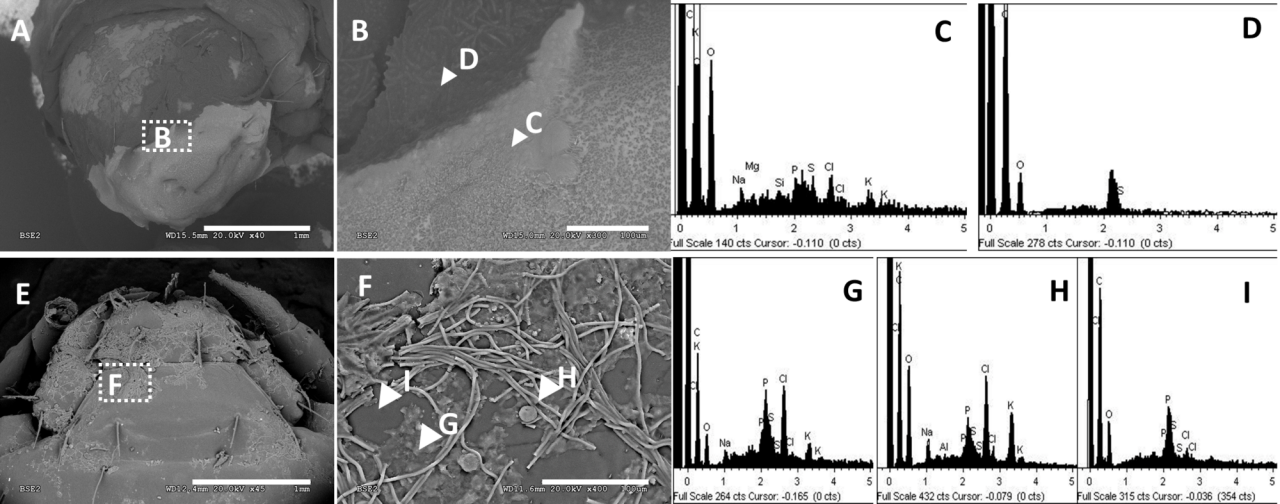
A
B
BSE2
WD15.5mm 20.0kV x40 1mm
B
D
C
BSE2
WD15.6mm 20.0kV x100 100um
C
C
K
O
Na
Mg
Si
P
S
Cl
K
K
0 1 2 3 4 5
ull Scale 140 cts Cursor: -0.110 (0 cts)
D
C
O
S
0 1 2 3 4 5
Full Scale 278 cts Cursor: -0.110 (0 cts)
E
F
BSE2
WD12.4mm 20.0kV x45 1mm
F
I
H
G
BSE2
WD11.6mm 20.0kV x400 100um
G
C
K
O
Na
P
S
Cl
K
K
0 1 2 3 4 5
Full Scale 264 cts Cursor: -0.165 (0 cts)
H
K
O
Na
Al
P
S
Cl
K
0 1 2 3 4 5
Full Scale 432 cts Cursor: -0.079 (0 cts)
I
C
O
P
S
Cl
Cl
0 1 2 3 4 5
Full Scale 315 cts Cursor: -0.036 (354 cts)

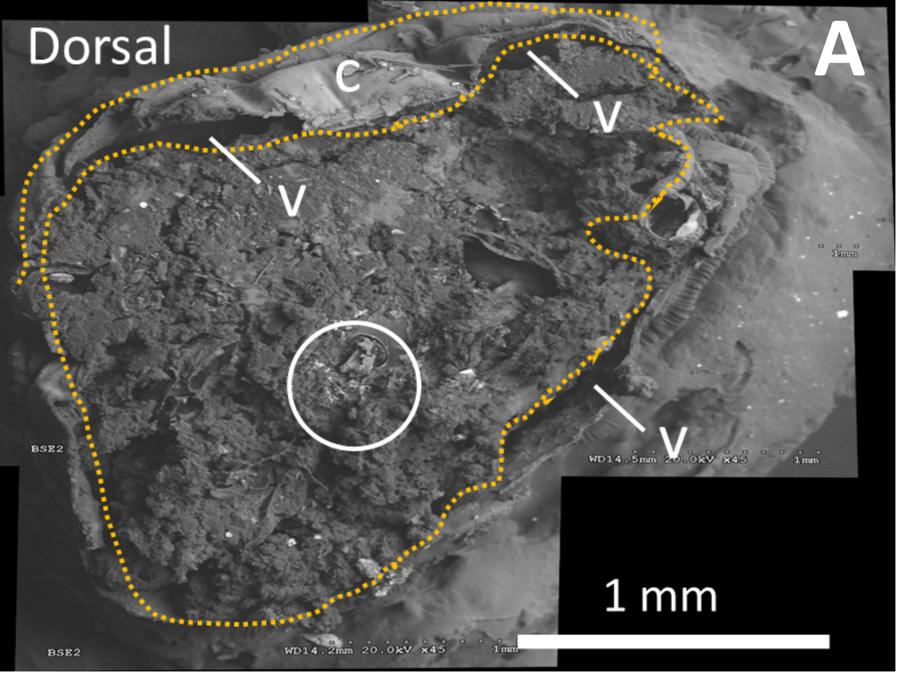
Dorsal
A
c
v
v
v
1 mm

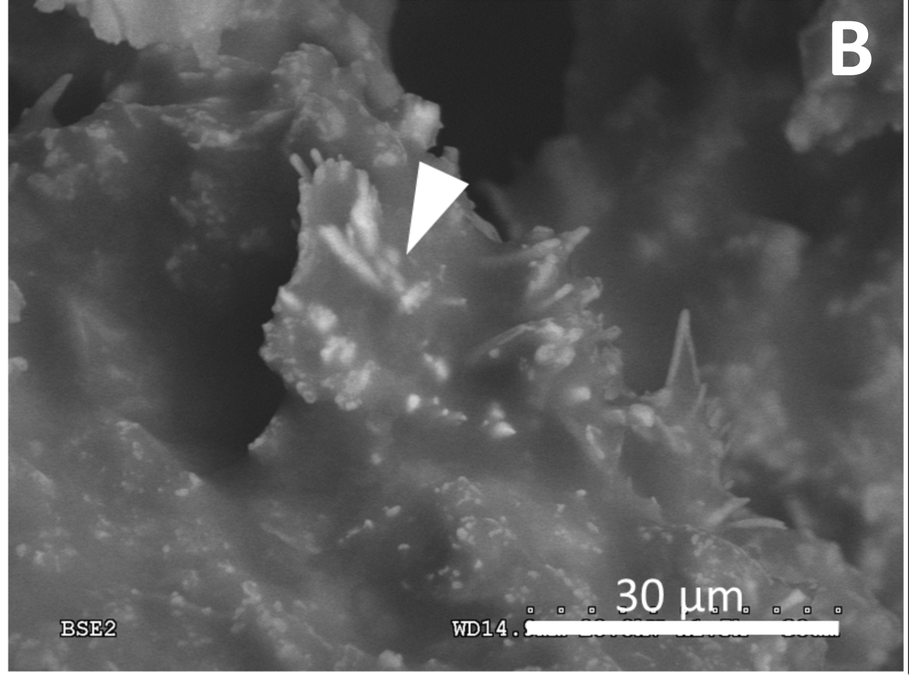
B
30 µm
BSE2

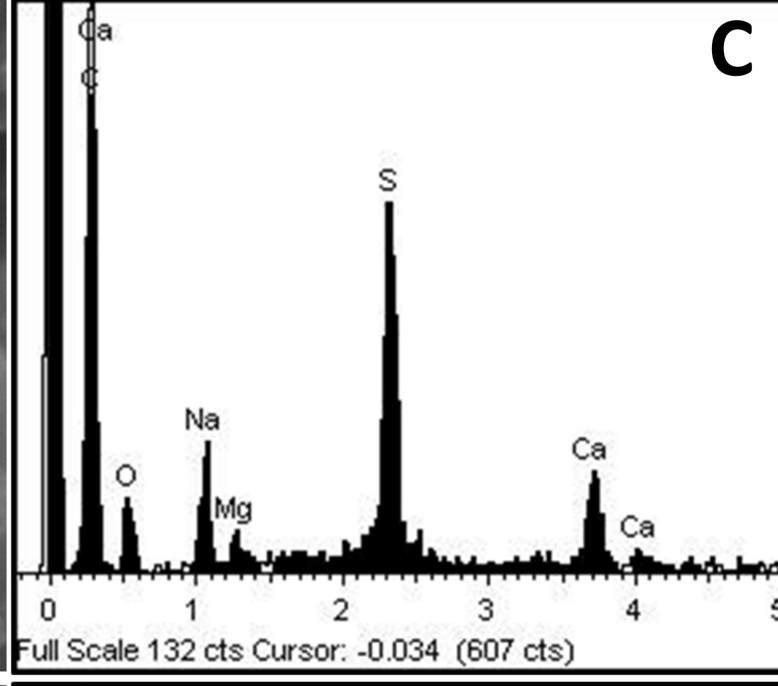
C
Ca
S
Na
O
Mg
Ca
Ca
0
1
2
3
4
Full Scale 132 cts Cursor: -0.034 (607 cts)

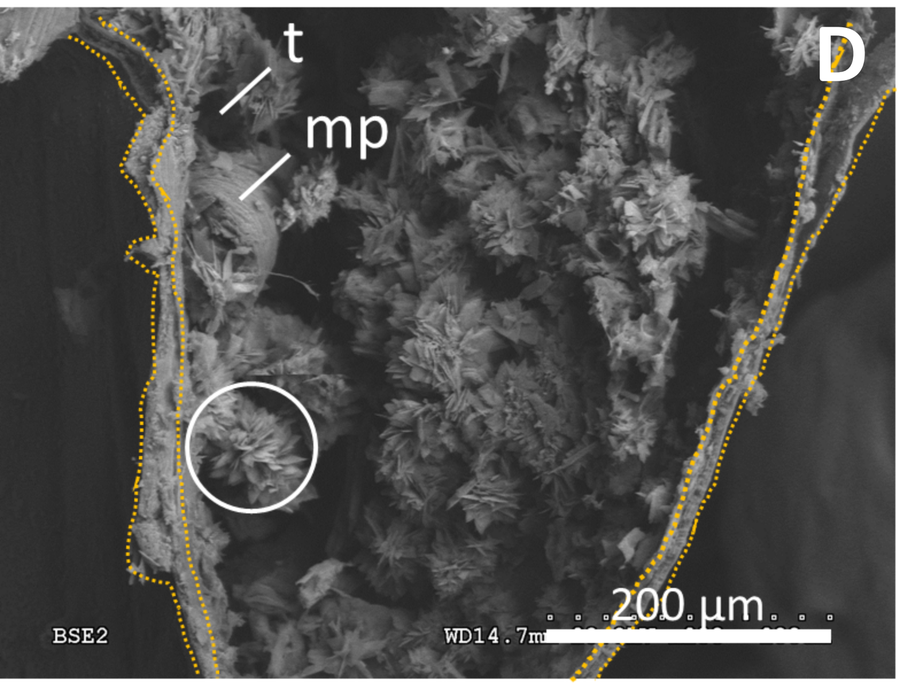
D
t
mp
200 µm
BSE2

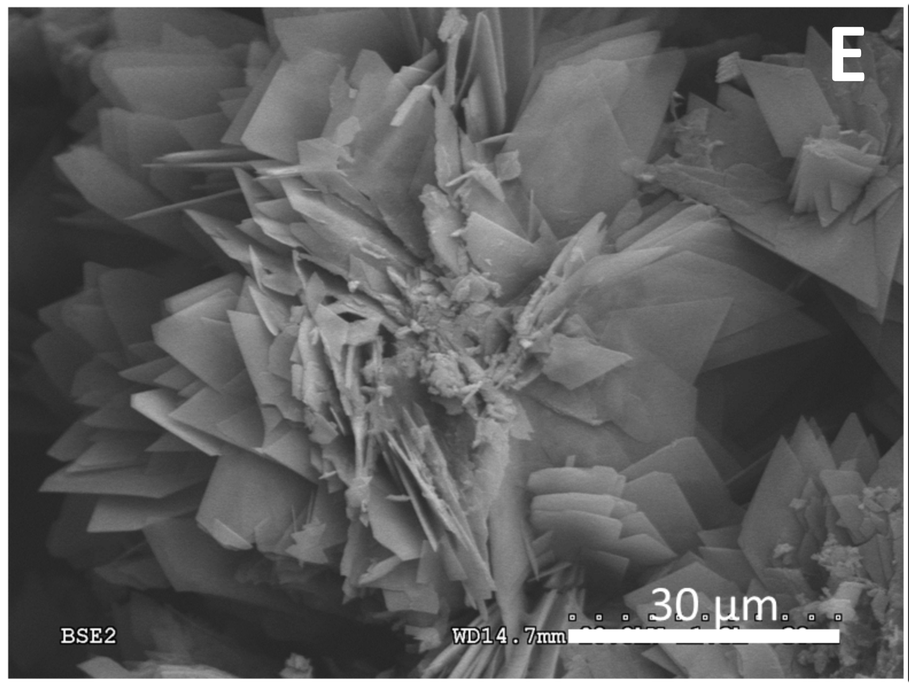
E
30 µm
BSE2

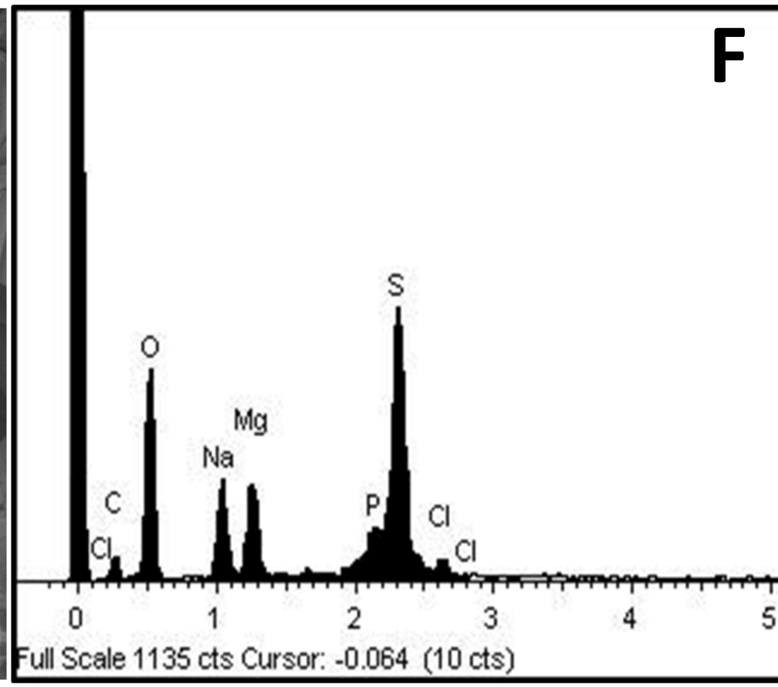
F
O
S
Mg
Na
C
Cl
P
Cl
Cl
0
1
2
3
4
5
Full Scale 1135 cts Cursor: -0.064 (10 cts)

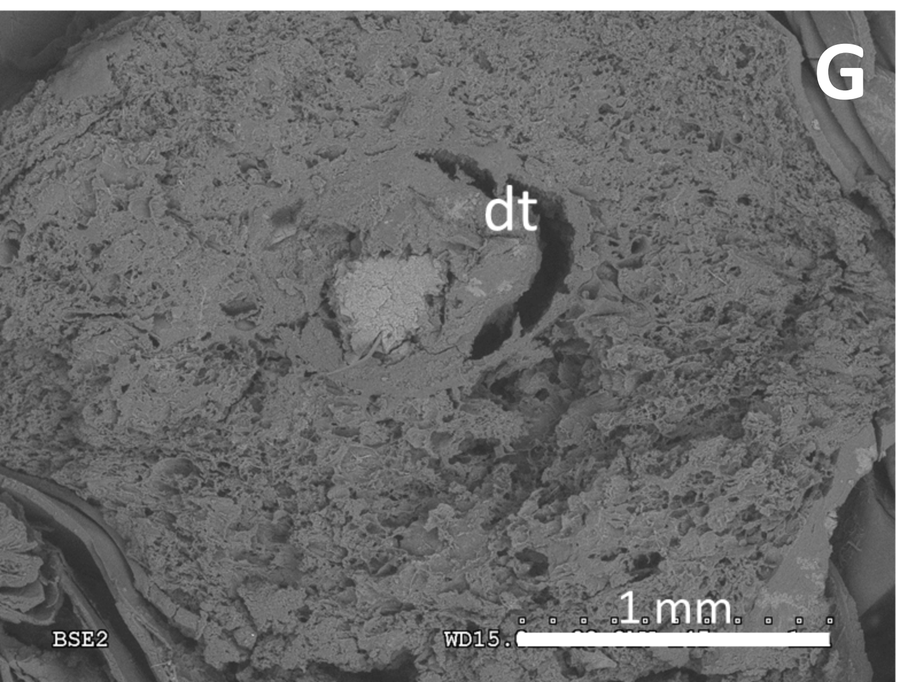
G
dt
1 mm
BSE2

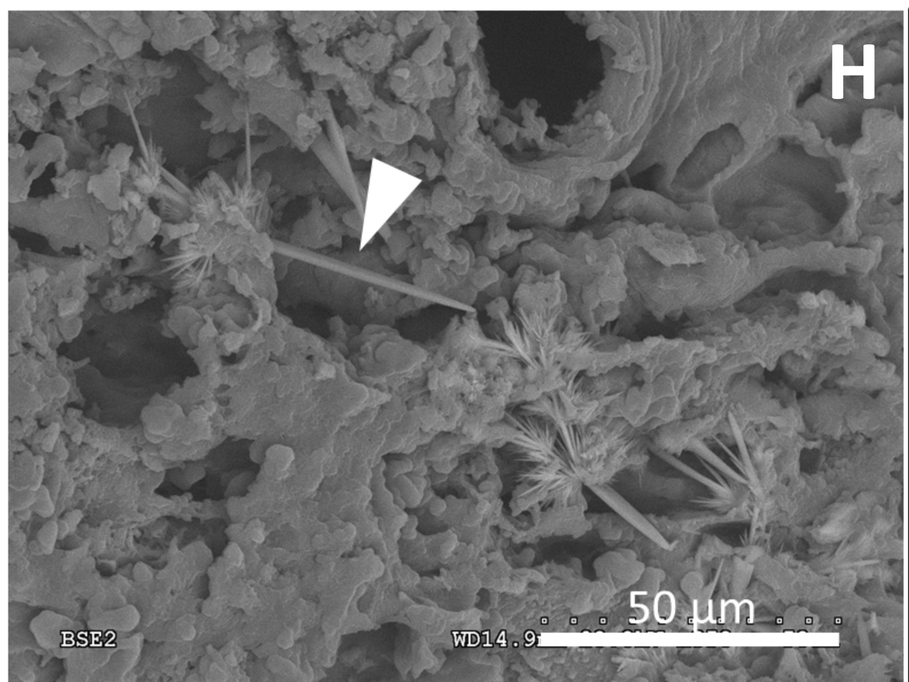
H
50 µm
BSE2

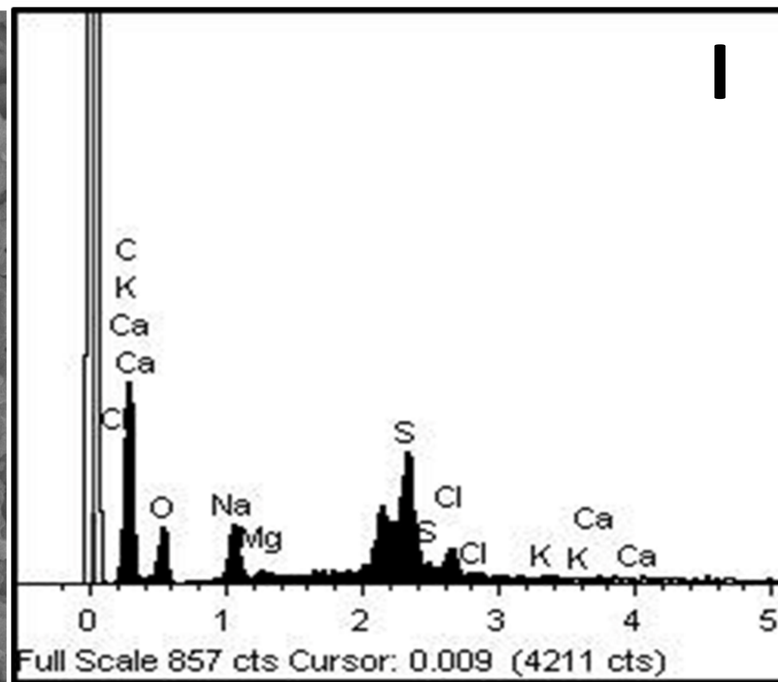
I
C
K
Ca
Ca
Cl
S
O
Na
Mg
Cl
S
Cl
K
K
Ca
Ca
0
1
2
3
4
5
Full Scale 857 cts Cursor: 0.009 (4211 cts)

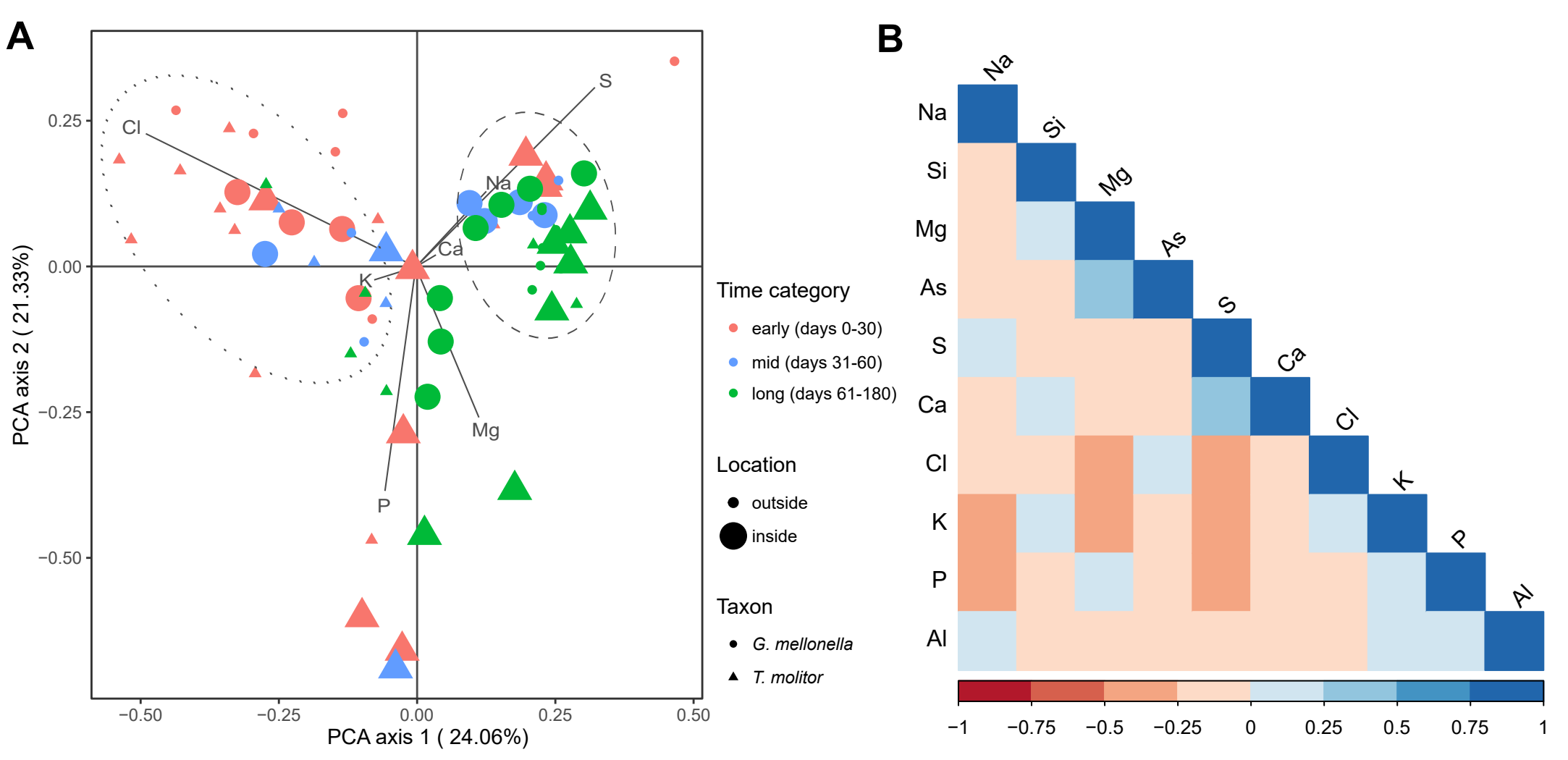
A
B
PCA axis 1 (24.06%)
PCA axis 2 (21.33%)
Cl
S
Na
Ca
K
Mg
P
Time category
early (days 0-30)
mid (days 31-60)
long (days 61-180)
Location
outside
inside
Taxon
G. mellonella
T. molitor
Na
Si
Mg
As
S
Ca
Cl
K
P
Al
−1
−0.75
−0.5
−0.25
0
0.25
0.5
0.75
1

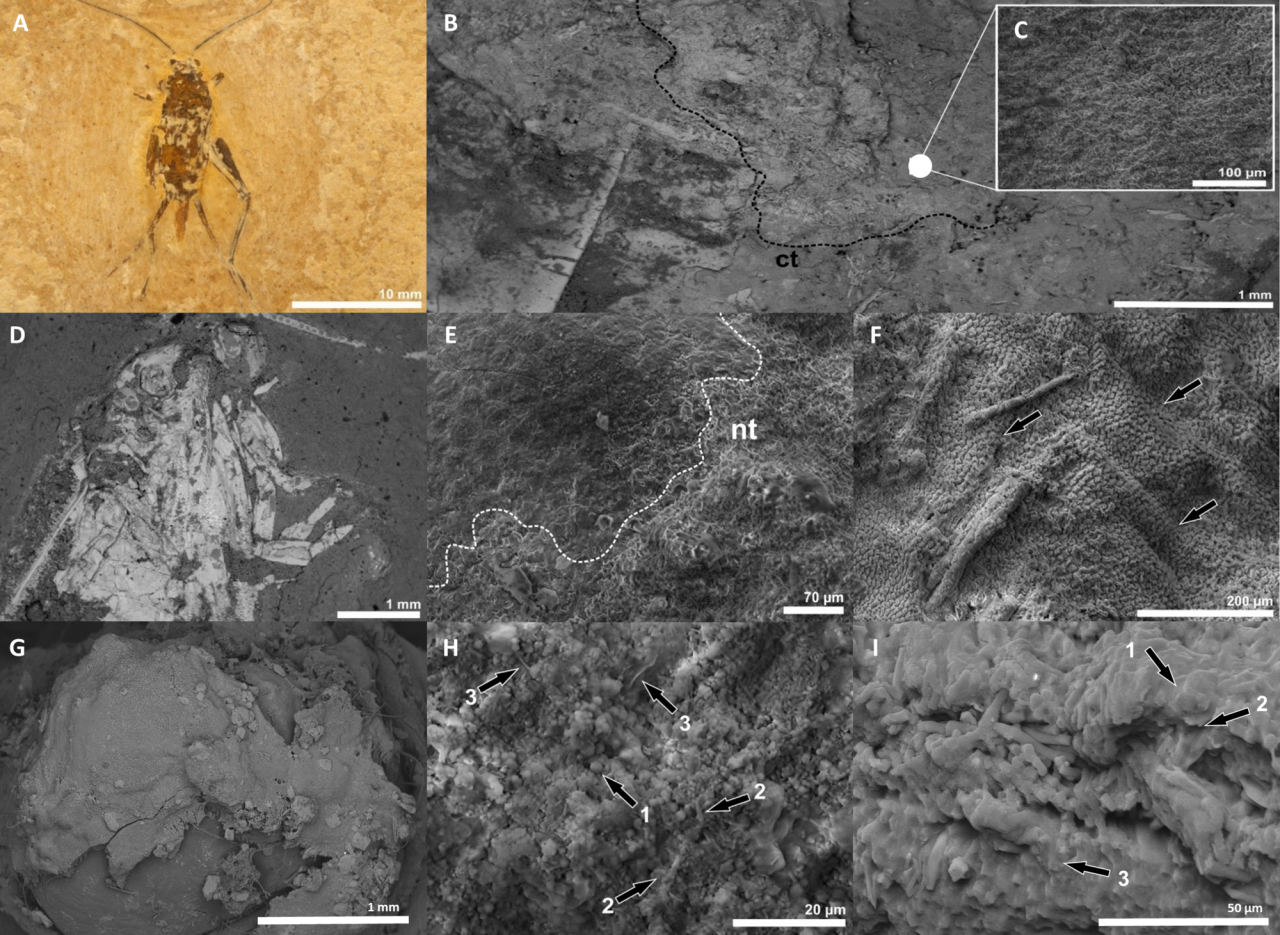
A
10 mm
B
ct
1 mm
C
100 µm
D
1 mm
E
nt
70 µm
F
200 µm
G
1 mm
H
3
3
1
2
2
20 µm
I
1
2
3
50 µm

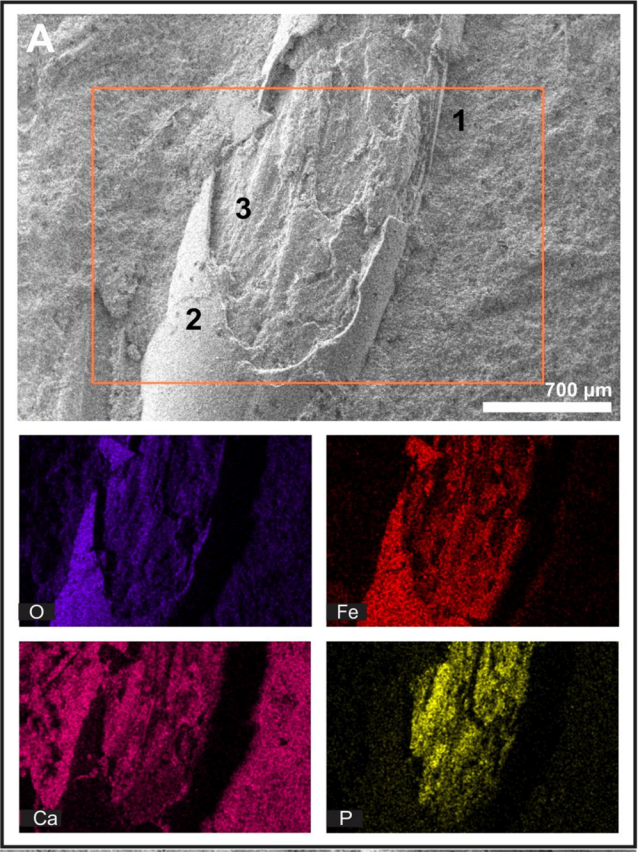
A
1
3
2
700 µm
O
Fe
Ca
P

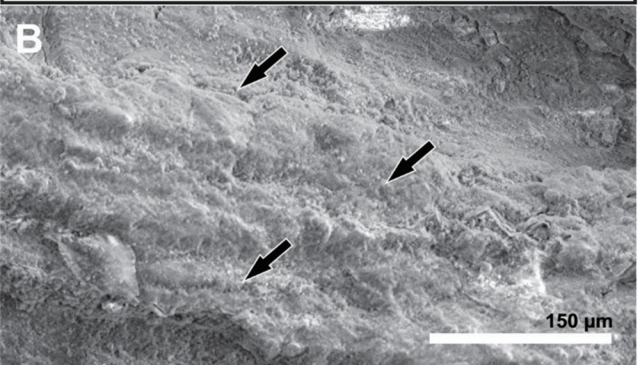
B
150 µm

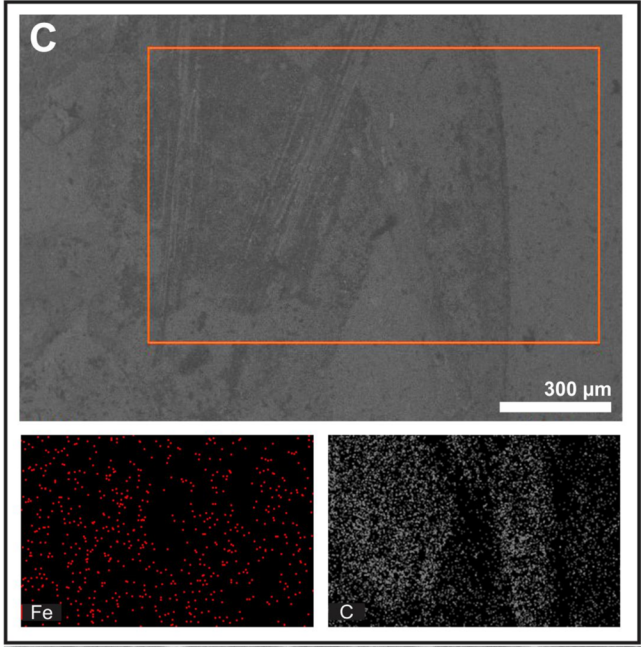
C
300 µm
Fe
C

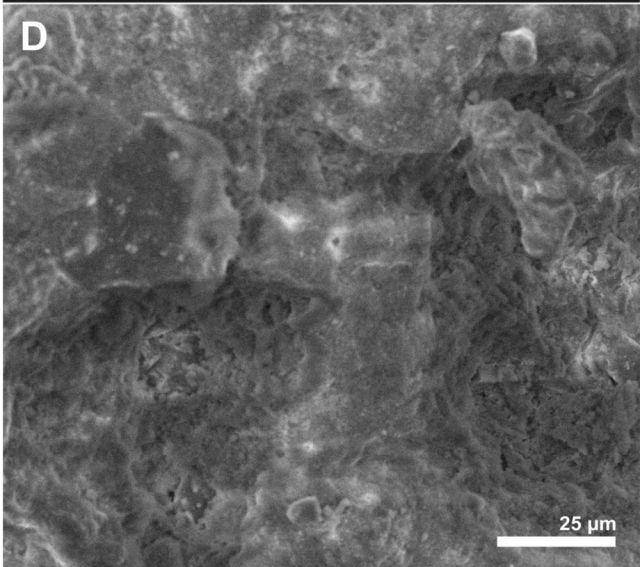
D
25 µm

Table 1: Soft tissue decay in *T. molitor*. The data Matrix shows the scores of the qualitative values assigned to the histological sections: Code (0), no obvious deterioration is observed; (1) slight deterioration of the structures, breaks or deformations, or appearance of bacteria in the coelom; (2) increase in the number of breaks, deformations, and the number of bacteria in the coelom; (3) fairly broken and deformed structures. More bacteria in the coelom than in state 2; (4) very pronounced deterioration, a large amount of bacteria in the coelom (see also figure S3 for the scores of the tissue decay). **Abbreviations**: C, control; d, day; Fl., floating initial phase; M, microbial mat; R., resting phase in which the carcass lay on the surface of the sediment/mat

Setting	**Experimental days**						**Observations**
Phase	Fl.	R.	----------Sarcophagus/Sediment----------				
	4d	**11d**	**30d**	**60d**	**120d**	**180d**	
M	0	0	0	0	1	2	Occurrence of microorganisms into body but outside the digestive tract
C	0	0	1	1	2	4	
M	0	0	0	0	1	1	Degradation of the cuticle
C	0	0	0	1	1	4	
M	0	1	1	1	2	3	Degradation of the fat bodies
C	0	1	2	3	4	4	
M	0	0	0	1	1	2	Degradation of the digestive tract
C	0	0	2	2	4	4	
M	0	0	1	1	2	3	Degradation of muscle packs
C	0	0	2	2	3	4	
M	0	0	0	0	0	1	Degradation of the trachea network
C	0	0	0	0	1	2	

Table 2: Soft tissue decay in *G. mellonella.* Data Matrix showing the scores of the qualitative values assigned to the histological sections: Code (0), no obvious deterioration is observed; (1) slight deterioration of the structures, breaks or deformations, or the appearance of bacteria in the coelom; (2) increase in the number of breaks, deformations, and the number of bacteria in the coelom; (3) Fairly broken and deformed structures. More bacteria in the coelom than in state 2; (4) very pronounced deterioration and a large amount of bacteria in the coelom (see also figure S3 for the scores of the tissue decay). **Abbreviations**: C, control; d, day; Fl., floating initial phase; M, microbial mat; R., resting phase in which the carcass lay on the surface of the sediment/mat

Setting							**Observations**
Phase	Fl.	R.	----------Sarcophagus/Sediment----------				
	4d	**11d**	**30d**	**60d**	**120d**	**180d**	
M	0	0	1	1	1	1	Occurrence of microorganisms into body but outside the digestive tract
C	0	0	1	2	3	3	
M	0	0	0	0	1	2	Degradation of the cuticle
C	0	0	1	2	2	3	
M	0	1	1	2	2	3	Degradation of the fat bodies
C	0	1	1	2	3	4	
M	0	0	1	1	1	3	Degradation of the digestive tract
C	0	0	0	1	2	3	
M	0	1	1	2	2	3	Degradation of muscle packs
C	0	1	1	2	3	4	
M	0	0	0	0	1	2	Degradation of the trachea network
C	0	0	0	2	3	4	
M	0	0	0	0	1	2	Degradation of the Silk glands
C	0	0	0	2	3	4	

Table 3: EDXS summary of the elemental composition over the course of the experiment (T1–T6). Values represent the average percentage (relative only to inorganic elements). Location (outside forming a crust or inside the carcasses) and taxa are shown. **Abbreviations**: d, day.

		Galleria mellonella							*Tenebrio molitor*						
		Na	**Mg**	**P**	**S**	**Cl**	**K**	**Ca**	**Na**	**Mg**	**P**	**S**	**Cl**	**K**	**Ca**
Outside	**4d T1**	20.9	10.4	16.4	16.4	19.4	10.4		12.7		14.2	10.8	45.8	16.3	
	11d T2				35.7	52.8	11.4		3.3	1.1	1.3	43.1	1.7	31.5	18.1
	30d T3	14.4	3.5		39.5	42.6			32.0	14.0		20.1	28.9		5.0
	60d T4	18	29.8		16.4	29.8	3.5		16.6	34.9		17.9	26.2		4.4
	120d T5	37.3	13.7	0.6	40.6	4.9	2.3	0.5							
	180d T6	23.6	28.5		42.1	3.8	0.5	1.3	10.3	31.6	0.5	27.0	12.0		11.8
Inside	**4d T1**	17.2	10.3	15.5	20.7	24.1	12.1			20.8	37.5	21.1	8.1	12.4	
	11d T2	32.4		12.2	17	35.2	3.1		19.6	16.6	18.6	20.9	21.8	2.3	0.3
	30d T3	41.2	4.7		2.7	49.4	2.0		61.2	4.3		31.2	2.8	0.5	
	60d T4	29.2	17.5		40.4	12.5	0.3		10.4	31.2	31.6	12.3	14.5		
	120d T5	42.6	13.4		33.0	11.0	0.6		25.6	35.5	11.3	26.6	0.3	0.2	
	180d T6	18.0	32.6	2.9	29.3	13.0		4.2	31.2	20.5	1.0	45.8	1.6		

Atomic % 0,2-9.9 10-19.9 20-29.9 >30